bioRxiv preprint doi: https://doi.org/10.1101/714337; this version posted July 25, 2019. The copyright holder for this preprint (which was not certified by peer review) is the author/funder, who has granted bioRxiv a license to display the preprint in perpetuity. It is made available under aCC-BY-NC-ND 4.0 International license.

Microglia are necessary for normal functional development of adult-born neurons in the olfactory bulb

Jenelle Wallace[1,2,3,4], Julia Lord[3], Lasse Dissing-Olesen[4,5], Beth Stevens[4,5,6,7,*], Venkatesh Murthy[1,2,3,*]

[1]Molecules, Cells, and Organisms training program

[2]Center for Brain Science, Harvard University, Cambridge, MA 02138, USA

[3]Department of Molecular & Cellular Biology, Harvard University, Cambridge, MA 02138, USA

[4]Boston Children's Hospital, F.M. Kirby Neurobiology Center, Boston, MA, USA

[5]Harvard Medical School, Boston, MA, USA

[6]Stanley Center for Psychiatric Research, Broad Institute of MIT and Harvard, Cambridge, MA, USA

[7]Howard Hughes Medical Institute, Boston Children's Hospital, Boston, MA, USA

*Correspondence: beth.stevens@childrens.harvard.edu (B.S.), vnmurthy@fas.harvard.edu (V.M.)

Abstract

Microglia play key roles in regulating synapse development and refinement in the developing brain, but it is unknown whether they are similarly involved during adult neurogenesis. By transiently ablating microglia from the healthy adult mouse brain, we show that microglia are necessary for the normal functional development of adult-born granule cells (abGCs) in the olfactory bulb. Microglia ablation reduces the odor responses of developing, but not preexisting GCs *in vivo* in both awake and anesthetized mice. Microglia preferentially target their motile processes to interact with mushroom spines on abGCs, and when microglia are absent, abGCs develop smaller spines and receive weaker excitatory synaptic inputs. These results suggest that microglia promote the development of excitatory synapses onto developing abGCs, which may impact the function of these cells in the olfactory circuit.

Introduction

Microglia are critically important for normal brain development in the embryonic and early postnatal stages (Hammond et al., 2018). Originally thought to be primarily involved in injury and disease, many recent studies have implicated microglia in diverse neurodevelopmental functions (Tremblay et al., 2011)(Salter and Beggs, 2014)(Wu et al., 2015)(Hong et al., 2016). However, much less is known about what role microglia might play in the healthy adult brain, even during the process of adult neurogenesis, which can be thought of as an extension of developmental processes throughout the lifespan.

During early postnatal development, microglia have been implicated in the regulation of synaptic development, including activity-dependent synaptic pruning (Stevens et al., 2007)(Schafer et

bioRxiv preprint doi: https://doi.org/10.1101/714337; this version posted July 25, 2019. The copyright holder for this preprint (which was not certified by peer review) is the author/funder, who has granted bioRxiv a license to display the preprint in perpetuity. It is made available under aCC-BY-NC-ND 4.0 International license.

al., 2012) (Paolicelli et al., 2011)(Gunner et al., 2019) on one hand and promotion of synaptic development and maturation on the other (Hoshiko et al., 2012)(Zhan et al., 2014)(Miyamoto et al., 2016)(Nakayama et al., 2018). Although microglia seem well-positioned to perform similar roles to facilitate the integration of adult-born neurons into circuits in the adult brain in the dentate gyrus (DG) and olfactory bulb (OB) (Ekdahl, 2012)(Rodríguez-Iglesias et al., 2019), most studies on microglial regulation of adult neurogenesis to date have focused on early stages of the process occurring in the neurogenic niches. For example, hippocampal adult neurogenesis is impaired in models of neuroinflammation (Monje et al., 2003)(Ekdahl et al., 2003) and in immune-deficient mice (Ziv et al., 2006). Microglia regulate adult neurogenesis in the subgranular zone of the DG through ongoing phagocytosis of apoptotic neuroblasts (Sierra et al., 2010), although they do not seem to be similarly involved in the subventricular zone (SVZ) or rostral migratory stream (RMS) (Kyle et al., 2019) (but see (Ribeiro Xavier et al., 2015)).

Most of what is known about microglial involvement in later stages of neurogenesis is based on injury and disease models. Microglial activation via sensory deafferentation in the OB decreases the number of adult-born neurons (Lazarini et al., 2012) and their spine density (Denizet et al., 2016). In addition, lipopolysaccharide injection or CX3CR1 knockout activates microglia in the hippocampus and alters both inhibitory (Jakubs et al., 2008) and excitatory (Bolós et al., 2018) synapses onto adult-born neurons in the DG. These studies suggest that microglia can modulate the synaptic integration of adult-born neurons under inflammatory conditions, but raise the question of whether they are similarly involved in the healthy adult brain.

A recent study documented increased activity in principal neurons in the OB after microglia ablation (Reshef et al., 2017). Here we investigate the cellular and circuit mechanisms behind this effect and demonstrate that microglia ablation reduces activity in adult-born granule cells (abGCs) that make inhibitory connections with principal cells in the OB. We show that microglia normally interact with spines in developing abGCs, and the volume of these spines is reduced when microglia are ablated. This is accompanied by a reduction in the amplitude of excitatory but not inhibitory inputs to abGCs, suggesting that microglia are essential for proper integration of abGCs in adult circuits.

Results

Microglia preferentially interact with mushroom spines on abGCs

We labeled cohorts of abGCs born within a short time window using lentiviral injection into the RMS (Consiglio et al., 2004)(Livneh and Mizrahi, 2012). To visualize interactions between microglia and

bioRxiv preprint doi: https://doi.org/10.1101/714337; this version posted July 25, 2019. The copyright holder for this preprint (which was not certified by peer review) is the author/funder, who has granted bioRxiv a license to display the preprint in perpetuity. It is made available under aCC-BY-NC-ND 4.0 International license.

abGCs, we performed time-lapse *in vivo* two-photon imaging of the dendrites of dTomato-labeled abGCs in the external plexiform layer (EPL) of the OB over the first four weeks after injection in CX3CR1-GFP +/- mice, in which microglia are labeled with GFP (Figure 1a). Consistent with previous observations (Nimmerjahn et al., 2005)(Tremblay et al., 2010), we found that microglial processes were highly motile and occasionally appeared in close proximity to labeled dendritic spines (Figure 1b). To quantify whether microglia preferentially interact with dendritic spines (defined as colocalization of a microglial process with a spine head, meaning the two are within the diffraction limit of our microscope) on abGCs compared to encountering them by chance during the course of continuous motility, we compared the frequency of interactions between microglial processes and spine heads in the actual imaging data with the frequency of interactions in an image in which the microglia channel was arbitrarily shifted with respect to the dendritic imaging channel ("Offset").

Microglia exhibited an impressive degree of motility, interacting with 38.0% of abGC dendritic spines classified as "mushroom" spines (Figure 1c) and 26.8% of spines classified as "filopodial" spines (Figure 1H) during the course of our 30-90 minute imaging sessions, which was slightly but not significantly higher than the percentages calculated in the offset data, 34.0% and 24.6%, respectively (Mushroom: Chi square test χ^2= 1.90, p = 0.17 and Filopodial: χ2= 0.29, p = 0.29). However, we found that microglia spent about twice as much total time interacting with mushroom spines in the real compared to the offset data (Data: median 0.24 min/10 min vs. Offset: 0.13 min/10 min, p = 0.02) (Figure 1d). An increase in the number of interactions (Data: 0.14 interactions/10 min vs. Offset: 0.09 interactions/10 min) was mostly responsible for this difference, since the number of interactions (p = 0.014) (Figure 1e) but not the length of the interactions (p = 0.80)(Figure 1f) was significantly higher than chance. There was no difference in the percent of the spine covered by the microglial process during the interaction (p = 0.93)(Figure 1g). In contrast, microglia did not interact with filopodial spines at levels above chance (Figure 1i-l).

These results suggest that microglia specifically interact with spines that likely contain functional synapses (Whitman and Greer, 2007), positioning them to influence synaptic stabilization and maturation during the early development of abGCs.

Odor responses are reduced in abGCs that mature in the absence of microglia

To assess whether microglial interactions are essential for the functional development of abGCs, we ablated microglia during the entire timecourse of abGC development, beginning three weeks before lentiviral labeling (Figure 2a). Microglial ablation using the CSF1R inhibitor PLX5622 formulated in chow

bioRxiv preprint doi: https://doi.org/10.1101/714337; this version posted July 25, 2019. The copyright holder for this preprint (which was not certified by peer review) is the author/funder, who has granted bioRxiv a license to display the preprint in perpetuity. It is made available under aCC-BY-NC-ND 4.0 International license.

as previously described (Elmore et al., 2014) efficiently ablated microglia from the OB (85% ablation as assessed by immunostaining, 96% ablation as assessed by FACS) within one week and ablation could be maintained at similar levels for up to nine weeks with ongoing delivery (Figure 2b, Figure 2—figure supplements 1 and 2).

At five to six weeks post injection, we used two-photon imaging to visualize abGC dendrites *in vivo*. Microglia ablation did not affect the overall number of adult-born neurons in the OB (Figure 2—figure supplement 3), consistent with other reports, (Reshef et al., 2017)(Kyle et al., 2019) and we could identify dTomato-labeled abGC dendrites with similar gross morphology in control and PLX-treated mice. We recorded calcium responses in abGC dendrites in anesthetized mice to a panel of 16 monomolecular odors (Table 1) while simultaneously imaging morphology in the dTomato channel to aid in region of interest identification and image alignment (Figure 2c). AbGC responses to odors were sparse as previously described (Figure 2d) (Wallace et al., 2017), but across the population we could identify dendrites responding to most of the odors in our panel (Figure 2e). We characterized responses by taking the mean $\Delta F/F_\sigma$ value across a five-second period following the onset of a two-second odor stimulus and plotted the cumulative distribution of dendritic responses across all odors. The distribution was shifted left towards lower responsiveness in PLX-treated mice ($p = 2.56e-08$) while the noise distributions constructed from blank trials were not different ($p = 0.96$)(Figure 2f). Dendrites in PLX-treated mice also responded to fewer odors (for threshold response criteria, see Methods) (Control: 2 odors, PLX: 1 odor, $p = 4.86e-04$) (Figure 2g). We also found that median lifetime sparseness (Willmore and Tolhurst, 2001) was decreased in dendrites in PLX-treated mice (Control: 0.18, PLX: 0.067, $p = 4.18e-04$), again suggesting a sparser representation of odors in PLX-treated mice (Figure 2h). These effects were also significant across mice, with lower median response amplitudes in PLX-treated mice (Control: 0.13, PLX: 0.067, $p = 0.048$) (Figure 2i). However, there was no difference in the median amplitude of responses above threshold (Control: 1.25, PLX: 1.32, $p = 0.76$) (Figure 2—figure supplement 4), suggesting that the difference in overall responses was mostly mediated by an increase in the proportion of dendrites that did not respond to any of the odors in our panel, which was significantly higher in PLX-treated mice (Control: 0.21, PLX: 0.35, $p = 0.030$) (Figure 2—figure supplement 4).

While imaging in anesthetized mice allows better control of breathing rate, brain motion, and possible motivational influences on brain state, granule cell odor representation is significantly different in awake mice (Kato et al., 2012)(Wienisch and Murthy, 2016)(Wallace et al., 2017). Therefore, we also imaged abGC dendrites in awake mice and found similar effects as in anesthetized mice (Figure 3A, Figure 3—figure supplement 1), with dendrites in PLX-treated mice having lower responsiveness (p =

bioRxiv preprint doi: https://doi.org/10.1101/714337; this version posted July 25, 2019. The copyright holder for this preprint (which was not certified by peer review) is the author/funder, who has granted bioRxiv a license to display the preprint in perpetuity. It is made available under aCC-BY-NC-ND 4.0 International license.

0.037) (Figure 3B), responding to a lower median number of odors (Control: 1, PLX: 0, p = 0.061) (Figure 3C) and having lower lifetime sparseness (Control: 0.067, PLX: 0, p = 0.069) (Figure 3C). Interestingly, while response timecourses were similar between control and PLX-treated mice in the anesthetized state (p = 0.30), allowing us to characterize responses with a simple mean across the odor analysis period, principal components analysis revealed different response time courses in awake mice (p = 0.004) (Figure 3—figure supplement 2). These differences were likely not due to changes in active sampling of odors since sniffing rates were not different during baseline or odor presentation periods (Baseline: Control = 3.49 Hz, PLX = 3.52 Hz, p = 0.91; Odor: Control = 4.00 Hz, PLX = 3.94 Hz, p = 0.81) (Figure 3—figure supplement 3). To ensure that our analysis of response amplitudes was not complicated by this possible change in response timing, we also applied an event detection analysis method to the awake data and found similar results (Figure 3—figure supplement 2) with dendrites in PLX mice still characterized by responses to a lower median number of odors (Control: 1, PLX: 0, p = 0.037) (Figure 3—figure supplement 2).

Microglia ablation after development has no effect on odor responses

We next wondered whether the effect of microglia ablation was specific to developing abGCs or whether it might affect abGCs more generally. To address this question, we modified our experimental timeline to label abGCs and wait three months for them to mature fully (Figure 4a) before imaging their responses to the same set of odors (Figure 4b) in the same mice before and after three weeks of PLX5622. In this case we found no significant differences in the distribution of responses (p = 0.89)(Figure 4c), median number of odors evoking a significant response (Control: 1, PLX: 1, p = 0.89) (Figure 4d), or lifetime sparseness (Control: 0.067, PLX: 0.067, p = 0.99). We verified that our imaging paradigm was stable since there was also no change in responses when we imaged the same mice for two sessions three weeks apart without any PLX treatment (Figure 4—figure supplement 1). Even after 9 weeks of PLX treatment, the level of responsiveness remained stable in mature abGCs (Figure 4—figure supplement 2).

Synapse development in abGCs that mature in the absence of microglia

Since we found that microglia ablation reduces the functional responses of abGCs, we wondered if there were accompanying changes in excitatory synapses made on abGCs. We first studied spines in the EPL since our *in vivo* imaging showed that microglia preferentially interact with mushroom spines in this area. Four weeks after lentiviral labeling, we examined spines on apical dendrites in abGCs in

bioRxiv preprint doi: https://doi.org/10.1101/714337; this version posted July 25, 2019. The copyright holder for this preprint (which was not certified by peer review) is the author/funder, who has granted bioRxiv a license to display the preprint in perpetuity. It is made available under aCC-BY-NC-ND 4.0 International license.

control and PLX-treated mice (Figure 5a,b). We found no significant difference in spine density (Control: 0.31 spines/µm, PLX: 0.42 spines/µm, p = 0.17) (Figure 5c), but the distribution of spine head volume was shifted towards smaller volumes in PLX-treated mice (p = 0.0044) (Figure 5d), although this did not reach significance when averaging across all spines in each cell (Control median: 0.39 μm^3, PLX median: 0.30 μm^3, p = 0.13).

We next investigated the electrophysiological correlates of the observed differences in spine head size by recording spontaneous excitatory postsynaptic currents (sEPSCs) in abGCs with the same timeline as our *in vivo* imaging experiments, namely microglia ablation three weeks before lentiviral labeling, continuing until electrophysiological recordings from labeled cells at five to six weeks post injection (Figure 6a,b). We found a similar frequency of sEPSCs in cells from control and PLX-treated mice (Control median: 31.7 Hz, PLX median: 31.3 Hz, p = 0.93) (Figure 6c), but their amplitude was reduced (Control median: 9.9 pA, PLX median: 8.6 pA, p = 0.019) (Figure 6c). Passive membrane properties including membrane resistance (Control: 597 MΩ, PLX: 532 MΩ, p = 0.31) and capacitance (Control: 14.2 pF, PLX: 13.6 pF, p = 0.61) were unchanged, signifying no differences in cell surface area or resting membrane properties (Figure 6—figure supplement 1). We also confirmed that our recording conditions were consistent by verifying that series resistance and the distance of the recorded cells from the mitral cell layer were not different between groups (Figure 6—figure supplement 1).

To check whether there might be accompanying changes in inhibition that could offset or augment the observed changes in excitation, we also recorded spontaneous inhibitory postsynaptic currents (sIPSCs) in the same cells (Figure 6e). We found no difference in the frequency (p = 0.76)(Figure 6f) or amplitude of sIPSCs (p = 0.39)(Figure 6F), suggesting that the observed differences in abGC functional responses are due to weaker excitatory inputs without noticeable accompanying changes in inhibition.

Microglia ablation after development has no effect on synaptic inputs

Since there was no significant change in functional responses in abGCs that matured before microglia ablation, we checked whether synaptic inputs were also unchanged in this condition using the same experimental timeline as before and recording sEPSCs in abGCs that experienced three weeks of microglia ablation after three months of maturation (Figure 7a). There was no significant change in the frequency (p = 0.21)(Figure 7b) or amplitude of sEPSCs (p = 0.68)(Figure 7c). Series resistance was similarly unchanged (Figure 7—figure supplement 1) as were inhibitory inputs (Figure 7—figure

bioRxiv preprint doi: https://doi.org/10.1101/714337; this version posted July 25, 2019. The copyright holder for this preprint (which was not certified by peer review) is the author/funder, who has granted bioRxiv a license to display the preprint in perpetuity. It is made available under aCC-BY-NC-ND 4.0 International license.

supplement 2). These results suggest that microglia ablation only affects synaptic inputs to abGCs when it occurs during the first five to six weeks of the cells' development rather than after maturation.

Discussion

We delineate an important role for microglia in the regulation of adult-born neuron integration in the healthy adult brain. Our study adds to the growing literature documenting significant physiological and/or behavioral effects following microglia ablation from the healthy adult brain (Parkhurst et al., 2013)(Torres et al., 2016)(Reshef et al., 2017). Importantly, our study is the first to link microglia ablation to changes in the *in vivo* activity and functional inputs of a specific affected cell population. We show that eliminating microglia has functional consequences for abGCs incorporating into the circuitry of the OB, reducing their responses to stimuli. Furthermore, we go on to investigate the physiological mechanisms and show that the dampened responses we observe are likely a consequence of reduced spine volume and weaker excitatory inputs in neurons that develop in the absence of microglia.

Methodological considerations

There are several technical caveats that must be acknowledged to allow proper interpretation of our study. While ablation of microglia with PLX5622 is highly efficient, it is unknown in what state the small remaining percentage of microglia may be. This is particularly relevant for adult neurogenesis because it is known that inflammation negatively regulates the integration of adult-born neurons. Encouragingly, there seems to be no upregulation of inflammatory markers with PLX treatment (Elmore et al., 2014)(Reshef et al., 2017). Furthermore, inflammation in the OB has been shown to generally affect adult-born neuron numbers (Lazarini et al., 2012) and spine density (Denizet et al., 2016) rather than specifically excitatory synapse strength as we show here, so it is unlikely that undetected inflammation relating to microglia ablation can account for the results we observe.

We also note that microglia ablation with PLX5622 is brain-wide. AbGCs receive local inputs from within the OB as well as feedback from other cortical areas and neuromodulatory inputs(Lepousez et al., 2013), so we cannot unambiguously attribute the effects on abGCs to changes within the OB. Future work will be necessary to investigate whether there is a change in the balance of distal (predominantly feedforward) and proximal (mostly feedback) inputs or instead a more general effect on excitatory synapse maturation and/or maintenance.

bioRxiv preprint doi: https://doi.org/10.1101/714337; this version posted July 25, 2019. The copyright holder for this preprint (which was not certified by peer review) is the author/funder, who has granted bioRxiv a license to display the preprint in perpetuity. It is made available under aCC-BY-NC-ND 4.0 International license.

Timing of microglia ablation

It should be noted that while our results suggest that the effect of microglia ablation is specific to developing abGCs since our results with microglia ablation after abGC development did not reach statistical significance in most cases, we saw similar trends in reduced responses and excitatory inputs regardless of the timing of microglia ablation. This could be because lentiviral labeling is an imperfect method for isolating a single cohort of abGCs (so some abGCs in the "after development group" may still be at an earlier stage of development – see discussion of newcomer cells in (Wallace et al., 2017)). Another possibility is that microglia ablation also affects mature abGCs, although to a lesser extent than developing abGCs. This could be because microglia may be involved in the general maintenance or strengthening of newly formed excitatory synapses in GCs, and even mature GCs have high rates of synapse formation (and elimination) compared to cells in other brain regions (Sailor et al., 2016). In this scheme, developing abGCs would demonstrate the most significant phenotype due to their higher rates of spine dynamics (Sailor et al., 2016), but even mature GCs might accrue smaller effects over time.

The larger effect of microglia ablation on developing rather than mature adult-born neurons highlights the role of microglia during developmental stages and may explain why some studies have not found significant effects of microglia ablation in other areas of the healthy adult brain (Elmore et al., 2014)(Torres et al., 2016).

Microglia-neuron interactions in the adult brain

Though several studies have examined microglial motility (Nimmerjahn et al., 2005) and interactions between microglia and neuronal elements (Wake et al., 2009)(Tremblay et al., 2010)(Sipe et al., 2016), it has not been rigorously established that microglia interact with synapses more often than would be expected by chance, given the dense synaptic milieu of the adult brain and the high degree of microglial process motility. Using automated methods to segment microglial processes from *in* vivo two photon time lapse imaging experiments and shuffle the resulting images for comparison, we demonstrated targeted motility towards mushroom spines on abGCs, which are likely to contain established excitatory synapses (Whitman and Greer, 2007). In the absence of microglia, these spines have reduced volume, and this corresponds to weaker excitatory synapses. Signaling through microglial CX3CR1 may be involved in microglial interactions with spines on abGCs (Zhan et al., 2014)(Reshef et al., 2017), but future work should investigate how this is related to the promotion of excitatory synapse strengthening. One possibility is that microglia may prune weaker synapses, allowing stronger synapses to strengthen further (Stevens et al., 2007)(Schafer et al., 2012) (Paolicelli et al., 2011). Consistent with

bioRxiv preprint doi: https://doi.org/10.1101/714337; this version posted July 25, 2019. The copyright holder for this preprint (which was not certified by peer review) is the author/funder, who has granted bioRxiv a license to display the preprint in perpetuity. It is made available under aCC-BY-NC-ND 4.0 International license.

this hypothesis, we observed a trend towards an increase in spine density in microglia-ablated animals, which is likely accounted for by filopodial spines which did not have functional or stable synapses (since we did not see an accompanying increase in the frequency of synaptic currents in PLX-treated mice). Although we did not directly observe pruning of dendritic spines in abGCs in our time lapse imaging experiments, it remains possible that microglia could prune presynaptic elements (Schafer et al., 2012)(Gunner et al., 2019)(which we did not image) or that our frame rate was too slow to observe such events (Weinhard et al., 2018). Alternatively, microglia may be involved in synaptic strengthening rather than pruning in this system through yet-uncovered mechanisms.

AbGCs in the olfactory circuit

AbGCs become responsive to odor stimuli soon after they arrive in the OB and then undergo a period of functional refinement during which their initially broadly tuned responses become more selective (Wallace et al., 2017). The fact that we observe reduced odor responses in six-week-old abGCs in microglia-ablated mice could suggest either a defect in synaptic formation and strengthening that begins early and persists throughout the cells' development or a period of normal development followed by a defect in synapse strengthening or refinement that causes fewer odor responses to be maintained at maturity. Further experiments tracking the timecourse of synaptic development and odor responses in microglia-ablated animals will be necessary to disambiguate these possibilities.

Consequences for olfactory processing

The reduced activity that we observe in mature abGCs after microglia ablation is consistent with increased activity in the principal cells they inhibit (Reshef et al., 2017). Since reduced inhibition from GCs to OB principal neurons has been directly linked to an increase in the time needed to discriminate odors in challenging olfactory tasks (Abraham et al., 2010), this alteration in the OB circuitry could have functional consequences (Egger and Urban, 2006). Furthermore, given that abGCs may have an outsized role in the plasticity that underlies complex olfactory behaviors (Breton-Provencher et al., 2009)(Li et al., 2018) (Mandairon et al., 2018), microglial regulation of their development may be crucial to ongoing plasticity in the olfactory system.

bioRxiv preprint doi: https://doi.org/10.1101/714337; this version posted July 25, 2019. The copyright holder for this preprint (which was not certified by peer review) is the author/funder, who has granted bioRxiv a license to display the preprint in perpetuity. It is made available under aCC-BY-NC-ND 4.0 International license.

Author contributions

JW performed two-photon imaging, electrophysiology, and confocal imaging experiments, analyzed the data, and prepared the figures. JW and JL performed spine quantification experiments (Figure 5). LDO performed flow cytometry experiments and analyzed flow cytometry data. JW, VM, and BS designed the study and wrote the manuscript. VM and BS supervised the work.

Acknowledgements

This work was supported by a grant from the NIH (R01 DC013329) to VNM. JLW was supported by the NSF GRFP (DGE1144152) and NRSA (F31 DC016482) from the NIDCD. BS was supported by NIH R01NS092578 and Merkin Award, Broad Institute. Microscopy on fixed tissue samples was performed at the Harvard Center for Biological Imaging where JLW was supported by the Simmons Family Award. We thank Martin Wienisch, Joseph Zak, Vikrant Kapoor, and Julien Grimaud from the Murthy lab for assistance with equipment setup and training in relevant techniques and the members of the Murthy and Stevens labs for productive discussions. Thanks to Arnaud Frouin and Alanna Carey from the Stevens lab for assistance with cloning and production of lentiviral plasmids. We thank Chen Wang and the Viral Core at Boston Children's Hospital for production of lentivirus.

bioRxiv preprint doi: https://doi.org/10.1101/714337; this version posted July 25, 2019. The copyright holder for this preprint (which was not certified by peer review) is the author/funder, who has granted bioRxiv a license to display the preprint in perpetuity. It is made available under aCC-BY-NC-ND 4.0 International license.

References

Abraham NM, Egger V, Shimshek DR, Renden R, Fukunaga I, Sprengel R, Seeburg PH, Klugmann M, Margrie TW, Schaefer AT, Kuner T. 2010. Synaptic inhibition in the olfactory bulb accelerates odor discrimination in mice. *Neuron* **65**:399–411. doi:10.1016/j.neuron.2010.01.009

Bolós M, Perea JR, Terreros-Roncal J, Pallas-Bazarra N, Jurado-Arjona J, Ávila J, Llorens-Martín M. 2018. Absence of microglial CX3CR1 impairs the synaptic integration of adult-born hippocampal granule neurons. *Brain Behav Immun* **68**:76–89. doi:10.1016/j.bbi.2017.10.002

Breton-Provencher V, Lemasson M, Peralta MR, Saghatelyan A. 2009. Interneurons produced in adulthood are required for the normal functioning of the olfactory bulb network and for the execution of selected olfactory behaviors. *J Neurosci* **29**:15245–15257. doi:10.1523/JNEUROSCI.3606-09.2009

Consiglio A, Gritti A, Dolcetta D, Follenzi A, Bordignon C, Gage FH, Vescovi AL, Naldini L. 2004. Robust in vivo gene transfer into adult mammalian neural stem cells by lentiviral vectors. *Proc Natl Acad Sci U S A* **101**:14835–14840. doi:10.1073/pnas.0404180101

Denizet M, Cotter L, Lledo P-M, Lazarini F. 2016. Sensory deprivation increases phagocytosis of adult-born neurons by activated microglia in the olfactory bulb. *Brain Behav Immun* 6–11. doi:10.1016/j.bbi.2016.09.015

Egger V, Urban NN. 2006. Dynamic connectivity in the mitral cell-granule cell microcircuit. *Semin Cell Dev Biol* **17**:424–432. doi:10.1016/j.semcdb.2006.04.006

Ekdahl CT. 2012. Microglial activation - tuning and pruning adult neurogenesis. *Front Pharmacol* **3**:41. doi:10.3389/fphar.2012.00041

Ekdahl CT, Claasen J, Bonde S, Kokaia Z, Lindvall O. 2003. Inflammation is detrimental for neurogenesis in adult brain **100**.

Elmore MRP, Najafi AR, Koike M a, Dagher NN, Spangenberg EE, Rice R a, Kitazawa M, Matusow B, Nguyen H, West BL, Green KN. 2014. Colony-stimulating factor 1 receptor signaling is necessary for microglia viability, unmasking a microglia progenitor cell in the adult brain. *Neuron* **82**:380–97. doi:10.1016/j.neuron.2014.02.040

Gunner G, Cheadle L, Johnson KM, Ayata P, Badimon A, Mondo E, Nagy MA, Liu L, Bemiller SM, Kim K, Lira SA, Lamb BT, Tapper AR, Ransohoff RM, Greenberg ME, Schaefer A, Schafer DP. 2019. Sensory lesioning induces microglial synapse elimination via ADAM10 and fractalkine signaling. *Nat Neurosci* **22**. doi:10.1038/s41593-019-0419-y

Hammond TR, Robinton D, Stevens B. 2018. Microglia and the Brain: Complementary Partners in

bioRxiv preprint doi: https://doi.org/10.1101/714337; this version posted July 25, 2019. The copyright holder for this preprint (which was not certified by peer review) is the author/funder, who has granted bioRxiv a license to display the preprint in perpetuity. It is made available under aCC-BY-NC-ND 4.0 International license.

Development and Disease. *Annu Rev Cell Dev Biol* **34**:523–544. doi:10.1146/annurev-cellbio-100616-060509

Hong S, Dissing-Olesen L, Stevens B. 2016. New insights on the role of microglia in synaptic pruning in health and disease. *Curr Opin Neurobiol* **36**:128–134. doi:10.1016/j.conb.2015.12.004

Hoshiko M, Arnoux I, Avignone E, Yamamoto N, Audinat E. 2012. Deficiency of the microglial receptor CX3CR1 impairs postnatal functional development of thalamocortical synapses in the barrel cortex. *J Neurosci* **32**:15106–11. doi:10.1523/JNEUROSCI.1167-12.2012

Jakubs K, Bonde S, Iosif RE, Ekdahl CT, Kokaia Z, Kokaia M, Lindvall O. 2008. Inflammation regulates functional integration of neurons born in adult brain. *J Neurosci* **28**:12477–88. doi:10.1523/JNEUROSCI.3240-08.2008

Kato HK, Chu MW, Isaacson JS, Komiyama T. 2012. Dynamic sensory representations in the olfactory bulb: modulation by wakefulness and experience. *Neuron* **76**:962–75. doi:10.1016/j.neuron.2012.09.037

Kyle J, Wu M, Gourzi S, Tsirka SE. 2019. Proliferation and Differentiation in the Adult Subventricular Zone Are Not Affected by CSF1R Inhibition. *Front Cell Neurosci* **13**:1–10. doi:10.3389/fncel.2019.00097

Lazarini F, Gabellec M-M, Torquet N, Lledo P-M. 2012. Early activation of microglia triggers long-lasting impairment of adult neurogenesis in the olfactory bulb. *J Neurosci* **32**:3652–64. doi:10.1523/JNEUROSCI.6394-11.2012

Lepousez G, Valley MT, Lledo P-M. 2013. The impact of adult neurogenesis on olfactory bulb circuits and computations. *Annu Rev Physiol* **75**:339–63. doi:10.1146/annurev-physiol-030212-183731

Livneh Y, Mizrahi A. 2012. Experience-dependent plasticity of mature adult-born neurons. *Nat Neurosci* **15**:26–8. doi:10.1038/nn.2980

Miyamoto A, Wake H, Ishikawa AW, Eto K, Shibata K, Murakoshi H, Koizumi S, Moorhouse AJ, Yoshimura Y, Nabekura J. 2016. Microglia contact induces synapse formation in developing somatosensory cortex. *Nat Commun* **7**:12540. doi:10.1038/ncomms12540

Monje ML, Toda H, Palmer TD. 2003. Inflammatory blockade restores adult hippocampal neurogenesis. *Science* **302**:1760–5. doi:10.1126/science.1088417

Nakayama H, Abe M, Morimoto C, Iida T, Okabe S, Sakimura K, Hashimoto K. 2018. Microglia permit climbing fiber elimination by promoting GABAergic inhibition in the developing cerebellum. *Nat Commun* **9**:1–2. doi:10.1038/s41467-018-05100-z

Nimmerjahn A, Kirchhoff F, Helmchen F. 2005. Resting microglial cells are highly dynamic surveillants of brain parenchyma in vivo. *Science* **308**:1314–8. doi:10.1126/science.1110647

bioRxiv preprint doi: https://doi.org/10.1101/714337; this version posted July 25, 2019. The copyright holder for this preprint (which was not certified by peer review) is the author/funder, who has granted bioRxiv a license to display the preprint in perpetuity. It is made available under aCC-BY-NC-ND 4.0 International license.

Paolicelli RC, Bolasco G, Pagani F, Maggi L, Scianni M, Panzanelli P, Giustetto M, Ferreira TA, Guiducci E, Dumas L, Ragozzino D, Gross CT. 2011. Synaptic pruning by microglia is necessary for normal brain development. *Science* **333**:1456–8. doi:10.1126/science.1202529

Reshef R, Kudryavitskaya E, Shani-Narkiss H, Isaacson B, Rimmerman N, Mizrahi A, Yirmiya R. 2017. The role of microglia and their CX3CR1 signaling in adult neurogenesis in the olfactory bulb. *Elife* **6**:1–30. doi:10.7554/eLife.30809

Ribeiro Xavier a. L, Kress BT, Goldman S a., Lacerda de Menezes JR, Nedergaard M. 2015. A Distinct Population of Microglia Supports Adult Neurogenesis in the Subventricular Zone. *J Neurosci* **35**:11848–11861. doi:10.1523/JNEUROSCI.1217-15.2015

Rodríguez-Iglesias N, Sierra A, Valero J. 2019. Rewiring of Memory Circuits: Connecting Adult Newborn Neurons With the Help of Microglia. *Front Cell Dev Biol* **7**:1–20. doi:10.3389/fcell.2019.00024

Sailor KA, Valley MT, Wiechert MT, Riecke H, Sun GJ, Adams W, Dennis JC, Sharafi S, Ming G, Song H, Lledo P-M. 2016. Persistent Structural Plasticity Optimizes Sensory Information Processing in the Olfactory Bulb. *Neuron* **91**:384–396. doi:10.1016/j.neuron.2016.06.004

Salter MW, Beggs S. 2014. Sublime Microglia: Expanding Roles for the Guardians of the CNS. *Cell* **158**:15–24. doi:10.1016/j.cell.2014.06.008

Schafer DP, Lehrman EK, Kautzman AG, Koyama R, Mardinly AR, Yamasaki R, Ransohoff RM, Greenberg ME, Barres B a, Stevens B. 2012. Microglia sculpt postnatal neural circuits in an activity and complement-dependent manner. *Neuron* **74**:691–705. doi:10.1016/j.neuron.2012.03.026

Sierra A, Encinas JM, Deudero JJP, Chancey JH, Enikolopov G, Overstreet-Wadiche LS, Tsirka SE, Maletic-Savatic M. 2010. Microglia shape adult hippocampal neurogenesis through apoptosis-coupled phagocytosis. *Cell Stem Cell* **7**:483–95. doi:10.1016/j.stem.2010.08.014

Sipe GO, Lowery, RL, Tremblay M-È, Kelly EA, Lamantia CE, Majewska AK. 2016. Microglial P2Y12 is necessary for synaptic plasticity in mouse visual cortex. *Nat Commun* **7**:10905. doi:10.1038/ncomms10905

Stevens B, Allen NJ, Vazquez LE, Howell GR, Christopherson KS, Nouri N, Micheva KD, Mehalow AK, Huberman AD, Stafford B, Sher A, Litke AM, Lambris JD, Smith SJ, John SWM, Barres B a. 2007. The classical complement cascade mediates CNS synapse elimination. *Cell* **131**:1164–78. doi:10.1016/j.cell.2007.10.036

Torres L, Danver J, Ji K, Miyauchi JT, Chen D, Anderson ME, West BL, Robinson JK, Tsirka SE. 2016. Brain , Behavior , and Immunity Dynamic microglial modulation of spatial learning and social behavior. *Brain Behav Immun* **55**:6–16. doi:10.1016/j.bbi.2015.09.001

bioRxiv preprint doi: https://doi.org/10.1101/714337; this version posted July 25, 2019. The copyright holder for this preprint (which was not certified by peer review) is the author/funder, who has granted bioRxiv a license to display the preprint in perpetuity. It is made available under aCC-BY-NC-ND 4.0 International license.

Tremblay M-È, Lowery RL, Majewska AK. 2010. Microglial interactions with synapses are modulated by visual experience. *PLoS Biol* **8**:e1000527. doi:10.1371/journal.pbio.1000527

Tremblay M-È, Stevens B, Sierra A, Wake H, Bessis A, Nimmerjahn A. 2011. The role of microglia in the healthy brain. *J Neurosci* **31**:16064–9. doi:10.1523/JNEUROSCI.4158-11.2011

Wake H, Moorhouse AJ, Jinno S, Kohsaka S, Nabekura J. 2009. Resting microglia directly monitor the functional state of synapses in vivo and determine the fate of ischemic terminals. *J Neurosci* **29**:3974–80. doi:10.1523/JNEUROSCI.4363-08.2009

Wallace JL, Wienisch M, Murthy VN. 2017. Development and Refinement of Functional Properties of Adult-Born Neurons. *Neuron* **96**:883–896. doi:10.1016/j.neuron.2017.09.039

Weinhard L, Di Bartolomei G, Bolasco G, Machado P, Schieber NL, Neniskyte U, Exiga M, Vadisiute A, Raggioli A, Schertel A, Schwab Y, Gross CT. 2018. Microglia remodel synapses by presynaptic trogocytosis and spine head filopodia induction. *Nat Commun* **9**. doi:10.1038/s41467-018-03566-5

Whitman MC, Greer C a. 2007. Synaptic integration of adult-generated olfactory bulb granule cells: basal axodendritic centrifugal input precedes apical dendrodendritic local circuits. *J Neurosci* **27**:9951–61. doi:10.1523/JNEUROSCI.1633-07.2007

Wienisch M, Murthy VN. 2016. Population imaging at subcellular resolution supports specific and local inhibition by granule cells in the olfactory bulb. *Sci Rep* **6**:29308. doi:10.1038/srep29308

Wu Y, Dissing-Olesen L, MacVicar BA, Stevens B. 2015. Microglia: Dynamic Mediators of Synapse Development and Plasticity. *Trends Immunol* **36**:605–613. doi:10.1016/j.it.2015.08.008

Zhan Y, Paolicelli RC, Sforazzini F, Weinhard L, Bolasco G, Pagani F, Vyssotski AL, Bifone A, Gozzi A, Ragozzino D, Gross CT. 2014. Deficient neuron-microglia signaling results in impaired functional brain connectivity and social behavior. *Nat Neurosci* **17**:400–6. doi:10.1038/nn.3641

Ziv Y, Ron N, Butovsky O, Landa G, Sudai E, Greenberg N, Cohen H, Kipnis J, Schwartz M. 2006. Immune cells contribute to the maintenance of neurogenesis and spatial learning abilities in adulthood. *Nat Neurosci* **9**:268–275. doi:10.1038/nn1629

bioRxiv preprint doi: https://doi.org/10.1101/714337; this version posted July 25, 2019. The copyright holder for this preprint (which was not certified by peer review) is the author/funder, who has granted bioRxiv a license to display the preprint in perpetuity. It is made available under aCC-BY-NC-ND 4.0 International license.

Materials and methods

Mice

Mice were C57BL/6J males (Jackson Laboratories) or CX3CR1-GFP heterozygotes (Jung et al., 2000) that were 8 to 12-weeks-old at the beginning of the experiment. Mice were singly housed after chronic cranial window implantation or housed with littermates for experiments that did not require an implant. In both cases, they were housed on a 12-hour reversed light/dark cycle after window implantation or viral injection. Littermates were randomly assigned to experimental groups (control vs. PLX). All procedures were performed using approved protocols in accordance with institutional (Harvard University Institutional Animal Care and Use Committee) and national guidelines.

Viral vectors

For all experiments involving lentiviral labeling of abGCs, we used a Tet-Off lentiviral system (Hioki et al., 2009) with one construct expressing the transactivator tTAad under control of a synapsin promotor (lenti-STB) and a second construct expressing structural and/or activity markers. For spine quantification in fixed tissue (Figure 5) and electrophysiology (Figures 6 and 7), we used lenti-STB and lenti-dTomato produced by the Boston Children's hospital. For imaging microglia-spine interactions (Figure 1), we used lenti-STB and lenti-dTomato-t2A-GCaMP5 and for all experiments measuring odor responses (Figures 2, 3 and 4) we used lenti-STB and lenti-dTomato-t2A-GCaMP6s produced in house. VSV-G pseudotyped lentiviral vectors were produced by transfection of human embryonic kidney cells (HEK293FT) with third-generation lentivirus plasmids using lipofection (Mirus TransIT®-293). Supernatant was collected 48 h after transfection and concentrated using ultrafiltration (Centricon Plus-20 PLGC centrifuge filter units).

Lentiviral injections and cranial window surgeries

Reproduced from (Wallace, Wienisch, & Murthy, 2017):
"Mice were anesthetized with an intraperitoneal injection of ketamine (100 mg/kg) and xylazine (10 mg/kg) and body temperature was maintained at 37°C by a heating pad. A small craniotomy was made bilaterally over the RMS injection sites (coordinates from bregma: A +3.3, L +0.82, from the brain surface: V-2.9 and -2.7) and 250 nL of lentivirus (1:1 mixture of both constructs or 1:50 dilution of the tTA-containing construct to achieve sparser labeling for spine quantification in Figure 5) was injected at each of the two depths using a pulled glass micropipette (tip diameter approximately 10-20 um)." For cranial windows, the surface of the brain was kept moist with artificial cerebrospinal fluid (125mMNaCl, 5mMKCl, 10mMGlucose, 10mMHEPES, 2mM CaCl2 and 2mM MgSO4 [pH 7.4]) and Gelfoam (Patterson Veterinary) and a glass window consisting of two 3 mm No. 1 coverslips (Warner) glued together with optical glue (Norland Optical Adhesive 61) was implanted as previously described (Adam and Mizrahi, 2011). For mice used for awake imaging, Kwik Sil (World Precision Instruments) was placed between the coverslip and the brain surface to reduce movement. In this case, the coverslip consisted of two 3 mm and one 4 mm No. 0 coverslips forming a plug (Dombeck & Tank, 2014) with the 4 mm coverslip cut to fit between the mouse's eyes. In both cases, the edges around the coverslip were sealed with Vetbond (3M) and then C&B-Metabond dental cement (Parkell, Inc.). A custom-made titanium headplate was cemented to the skull. After surgery, mice were treated with carprofen (6 mg/kg) every 24 hours and buprenorphine (0.1 mg/kg) every 12 hours for 5 days."

bioRxiv preprint doi: https://doi.org/10.1101/714337; this version posted July 25, 2019. The copyright holder for this preprint (which was not certified by peer review) is the author/funder, who has granted bioRxiv a license to display the preprint in perpetuity. It is made available under aCC-BY-NC-ND 4.0 International license.

Two photon imaging of microglia-spine interactions (Figure 1)

A custom-built two-photon microscope (Wienisch et al., 2012) was used for in vivo imaging. Fluorophores were excited and imaged with a water immersion objective (20x, 0.95 NA, Olympus) at 950 nm using a Ti:Sapphire laser (Mai Tai HP, Spectra-Physics). The point spread function of the microscope was measured to be 0.66 x 0.66 x 2.26 µm. Image acquisition and scanning were controlled by custom-written software in Labview. Emitted light was routed through two dichroic mirrors (680dcxr, Chroma and FF555- Di02, Semrock) and collected by two photomultiplier tubes (R3896, Hamamatsu) using filters in the 500-550 nm range (green channel, FF01-525/50, Semrock) and 572-642 nm range (red channel, FF01-607/70, Semrock). Fields of view were 75x75 µm square spanning 800x800 pixels. Z-stacks of approximately 30 µm depth with a 1 µm z step for both channels (16 bit) were taken every 3 minutes (0.5 Hz frame rate with 3x averaging during acquisition) for periods of 30-90 minutes. Two or three fields of view were imaged in each mouse.

Analysis of microglia-spine interactions (Figure 1)

Since both channels exhibited bleed-through with our imaging parameters, the ImageJ spectral unmixing plugin (Author: J. Walter) was used to calculate and apply unmixing matrices for each image stack prior to further analysis. In Fiji, spine heads were delineated manually for each time point in the frame where they appeared brightest using the oval or polygon tools and ROI Manager and classified as either mushroom (spines whose spine head was wider than the spine neck at all timepoints) or filopodial (without a well-defined head). The Weka segmentation plugin (Arganda-Carreras et al., 2017) was used to perform binary segmentation of microglial processes from background after training on 5 frames (that were fully segmented manually) selected to represent a variety of microglial morphologies and brightness variation across the three mice. To optimize our resolution, we segmented very conservatively by using z stacks to mark microglial processes only in the plane where they appeared brightest. This strategy combined with only delineating spine heads in the brightest frame means that we only detected the closest interactions between microglial processes and spine heads. The features chosen for segmentation training in Weka were Gaussian blur, Sobel filter, Hessian, and Difference of Gaussians. This approach allowed us to segment complex microglia morphology from background automatically in every image frame and obviated the need for corrections for bleaching or variations in brightness across different imaging fields. Imaging frames that were too dim to segment (usually due to loss of immersion water) were excluded. Each segmented image stack was checked manually to ensure that any residual bleed-through from the red channel did not appear in the segmentation. After segmentation, ROIs representing spine heads were loaded onto the segmented image and the measured mean value within each ROI at each timepoint (0 if there was no colocalization or up to 1 if all pixels were colocalized with a segmented microglial process) was measured and exported into Matlab for further analysis. For offset data, we took the same segmented image stack and translated it horizontally by half the total number of pixels before measuring the overlap with the same spine head ROIs. To produce Video 2, frames were first registered with the MultiStackReg plugin (Author: Brad Busse) based on the magenta channel and bleaching was corrected with histogram matching in ImageJ (these steps were not necessary for analysis because we segmented each image frame separately as described above).

Two photon imaging of odor-evoked responses (Figures 2 and 4)

Reproduced from (Wallace, Wienisch, & Murthy, 2017):

bioRxiv preprint doi: https://doi.org/10.1101/714337; this version posted July 25, 2019. The copyright holder for this preprint (which was not certified by peer review) is the author/funder, who has granted bioRxiv a license to display the preprint in perpetuity. It is made available under aCC-BY-NC-ND 4.0 International license.

"Animals were anesthetized with an intraperitoneal injection of ketamine and xylazine (90% of dose used for surgery) and body temperature was maintained at 37°C by a heating pad. Frame rates were 4 Hz, the pixel size was 0.5 µm, and fields of view measured 150 x 150 µm. To locate regions for imaging, a low magnification z stack (~300-500 µm square) at slow scanning speed (usually 0.5 Hz) with a 1-2 µm z step was taken from the surface of the dura to the granule cell layer. Planes with many dendrites perpendicular to the imaging axis were chosen for imaging during odor stimulation."

Two photon imaging in awake animals (Figure 3)

Animals were water-restricted beginning 1-2 days before being handled and accustomed to head-fixation in a restraining tube (Guo et al., 2014) for 1-2 days with manual delivery of water rewards (approximately 30 minute sessions each). They were then acclimated to the sound of the scan mirrors and odor delivery (using the full odor set) on the day before imaging with manual delivery of water rewards before imaging and periodically between sets of repetitions. The same protocol was repeated for 1 or 2 days of imaging for each mouse.

Odor stimulation

Odor lists are found in Table 1. Odors (Sigma) were delivered with a custom-built 16 channel olfactometer at a nominal volumetric concentration of 16 % (v/v) in mineral oil and further diluted by 16 times in air to a final concentration of approximately 1% (except for isoeugenol which was not diluted in the olfactometer and therefore had a final concentration of approximately 6.25%). Odors were presented for 2 s with an interstimulus interval of 40 s with 3-5 times repetitions. The order of odor delivery was not randomized. A "no odor" trial with the same parameters but in which no odor valve opened was included with each set of repetitions. Odors were delivered through a mask with balanced input and output air flow that also allowed us to record respiration (Grimaud & Murthy, 2018). The positioning of the mask was adjusted daily to ensure optimal signal to noise. A photoionization detector (miniPID, Aurora Scientific) was used to confirm that odor concentrations were consistent between trials with these parameters. Odors were replaced before each set of experiments.

In vivo imaging analysis (Figures 2, 3, 4)

Data were analyzed offline using custom-written scripts in MATLAB (Mathworks). Experimenters were blind to fluorescence changes during data analysis but not to experimental group.

Regions of interest (ROIs)

Dendritic ROIs from abGCs were chosen based on average intensity projections in the dTomato channel as previously described (Wallace et al., 2017). Fields of view were non-overlapping and separated by at least 100 µm to minimize the chance of the same dendrites appearing in multiple fields of view. Z stacks of each imaging region were taken with a 2 µm z step from the surface of the dura down to the convergence of GC dendrites into a single apical dendrite. The density of labeling precluded tracing of all dendrites back to their parent cell, but we used these z stacks to ensure that multiple ROIs were not chosen from the same dendrite. Therefore, these data should be considered a sample from a population of dendrites rather than cells since some dendrites may have originated from the same cell. For ablation in abGCs after development (Figure 4), the same fields of view were imaged before and after PLX treatment. For Figure 4—Supplement 2, we chose matching ROIs for the two sessions (any ROIs without similar morphology between the two sessions were excluded as described previously (Wallace et al., 2017)) to quantify how much our imaging conditions changed between sessions without PLX treatment.

bioRxiv preprint doi: https://doi.org/10.1101/714337; this version posted July 25, 2019. The copyright holder for this preprint (which was not certified by peer review) is the author/funder, who has granted bioRxiv a license to display the preprint in perpetuity. It is made available under aCC-BY-NC-ND 4.0 International license.

However, we opted to choose ROIs independently for Figure 4 since matching ROIs always results in the exclusion of many ROIs, reducing sample size.

Motion correction

To correct for fast lateral motion and image drift, all image frames for a given field of view were aligned to the average of the first trial using cross-correlation based on rigid body translation (ImageJ plugin Moco)(Dubbs, Guevara, & Yuste, 2016). Frames with out of frame motion were removed based on the cosine similarity between each frame and the average intensity projection of the first trial (or the user-determined trial with the least motion for awake imaging). Image frames with cosine similarity that differed by more than 25% (30% for awake imaging) from the mean value for the user-determined best trial for that field of view or more than 20% (15% for awake imaging) from the mean of the baseline period for that trial were discarded. In some trials, immersion water dried up or laser power fluctuated, so trials were removed if their average brightness was less than half of the brightness of the average of the first three trials or if difference in brightness between the baseline and odor periods was greater than three times the standard deviation of brightness in the first trial. The entire trial was removed if, after these corrections, it contained less than 75% of the original frames during either the baseline or odor analysis period.

Fluorescence changes

The average intensity in the GCaMP channel was calculated for each ROI, for each frame and for each odor. A response value for each cell-odor pair was calculated as the average $\Delta F/F_\sigma$ value over the odor analysis period (5 s following odor onset) where F_σ represents the standard deviation of fluorescence during the baseline period. We used F_σ because we found that in many cases the baseline GCaMP6s fluorescence was so low in abGC dendrites that we could not reliably subtract the background as described previously (Wallace et al., 2017). Bleaching was corrected by fitting a single exponential to the florescence during the baseline period and taking the value at the end of the baseline period as the baseline mean, only for ROIs where the fluorescence during the last 2.5 s of the baseline period was greater than 1.1 times the fluorescence during the first 2.5 s. If, after correction for bleaching, baseline F_σ was greater than 30% of the mean baseline fluorescence, that ROI was considered too noisy and was removed from the analysis.

Event analysis (Figure 3—Supplement 2)

Events were detected separately in each trace using the calculated ROC threshold (see next section) and any frames that were included in an event in any repeat were averaged across all repeats to obtain a mean event trace and the mean value in a 1 second period around the peak in this mean trace was then calculated. For latency, the mean latency across repeats was calculated for all repeats that had detected events.

Thresholds

For all figures where a threshold was applied to the data, thresholds were calculated based on the distribution of “no odor” trials. An area under the receiver operating curve analysis was performed and the lowest threshold yielding a 10% false positive rate was chosen. Thresholds were calculated for each figure by combining responses from both control and PLX-treated groups and performing ROC analysis on the combined data. For event detection, we used ROC analysis to find the optimal combined threshold for the number of frames and standard deviation above baseline and chose the threshold that gave closest to a 10% false positive rate.

Lifetime sparseness

bioRxiv preprint doi: https://doi.org/10.1101/714337; this version posted July 25, 2019. The copyright holder for this preprint (which was not certified by peer review) is the author/funder, who has granted bioRxiv a license to display the preprint in perpetuity. It is made available under aCC-BY-NC-ND 4.0 International license.

After applying a threshold to the data, we used the following equation to calculate lifetime sparseness: (Willmore and Tolhurst, 2001)

$$LS = \frac{\left(\sum_{j=1}^{m} \frac{r_j}{m}\right)^2}{\left(\sum_{j=1}^{m} \frac{r_j^2}{m}\right)}$$

where m = number of odors, r_j = response of the neuron to odor j.

If all stimuli activate a cell nearly uniformly, LS will be close to 1, and if only a small fraction of the stimuli activate a cell significantly, LS will be close to 0. For any cells with all responses below threshold, we set LS = 0, interpreting this as the sparsest possible representation.

Temporal dynamics

Principal component analysis of the time course of responses was performed in Matlab using centered data and singular value decomposition as described previously (Wienisch & Murthy, 2016). To compare timecourses for the control and PLX-treated groups, principal components were calculated on each dataset (all traces from all cell-odor pairs) separately and the angle between the two spaces spanned by the coefficient vectors for the first three principal components from the beginning to the end of the odor analysis period was calculated. Then the group to which each trace belonged was shuffled 1,000 times, and the angles between new coefficient vectors were calculated based on random division into two groups of the same size as the original datasets. The actual angle was then compared to this distribution to obtain a p value.

Respiration measurements

Peaks were extracted from respiration traces using the findPeaks function in Matlab with a minimum peak distance of 10 Hz.

Raincloud plots

Raincloud plots of the type in Figure 2G were created using the Matlab version of the RainCloudPlots package (Allen, Poggiali, Whitaker, Marshall, & Kievit, 2018).

Microglia ablation with CSF1R inhibitor PLX5622

CSF1R inhibitor PLX5622 was generously provided by Plexxikon (Berkeley, CA) and mixed into standard rodent diet at 1200 mg per kilogram of chow (Research Diets: AIN-76A diet). Control diet was formulated identically, but without the inhibitor.

Flow Cytometry (Figure 2--Supplement 1)

Microglia ablation was confirmed via flow cytometry. A single cell suspension enriched for microglia was generated as previously described (Hammond et al., Immunity 2019). Briefly, mice were deeply anesthetized with a mixture of ketamine (100 mg/kg) and xylazine (10 mg/kg) and transcardially perfused with 20 mL of cold Hank's balanced salt solution (HBSS, GIBCO, 14175-079). Bulbs and brains were minced using a razor blade (Electron Microscopy Science, 71960) and homogenized using a dounce tissue grinder (Wheaton, 357542). Microglia were enriched via centrifugation in 40% Percoll (Sigma-Aldrich, 17-0891-01) at 500g for 1h at 4°C. Samples were incubated for 20 min with Blue Dead Cell Stain (Thermo Fisher, L34961) and Fc blocking antibody (Rat Anti-Mouse CD16/CD32, BD Bioscience, 553141) in HBSS + 2 mM EDTA. Cells were additionally stained for 20 min with antibodies against CD45 (Biolegend, 103116) and CD11b (Biolegend, 101217) in FACS buffer (HBSS + 2 mM EDTA + 0.5% BSA).

bioRxiv preprint doi: https://doi.org/10.1101/714337; this version posted July 25, 2019. The copyright holder for this preprint (which was not certified by peer review) is the author/funder, who has granted bioRxiv a license to display the preprint in perpetuity. It is made available under aCC-BY-NC-ND 4.0 International license.

Counting Beads (CountBright, Thermo Fisher Scientific, C36950) were added and samples analyzed using a FACS Aria II 'SORP'. All events were collected until a total of 8000 counting beads had been acquired for each sample. The data were analyzed in FlowJo 10.2.

BrdU injections (Figure 2—Supplement 3)

Mice received two intraperitoneal injections of BrdU (100 mg/kg in 0.9% saline) 12 hours apart.

Fixed tissue preparation

Mice were deeply anesthetized with a ketamine/xylazine mixture and perfused transcardially with 20 mL of PBS (pH 7.4) first, followed by 30-50 mL of 4% paraformaldehyde (diluted from 16% stock, Electron Microscopy Sciences) in 0.1 M phosphate buffered saline (pH 7.4). Brains were removed from the skull and placed in 5 ml 4% paraformaldehyde for 2 hours. They were then rinsed with PBS and one hemisphere for each mouse was sliced coronally at 100 µm with a vibratome (Leica) for imaging of dTomato-labeled abGC spines (Figure #), while the other hemisphere was sliced sagitally at 35-40 µm for immunostaining (Iba, Figure # or BrdU, Figure #).

Immunohistochemistry

For Iba-1 staining, 3-4 slices per mouse spanning the olfactory bulb were permeabilized and blocked with a solution containing 0.1% Triton X-100 (Fisher), and 5% goat serum in PBS for 1 hour at room temperature or blocked with Starting Block (ThermoFisher) with 0.3% TritonX-100 for 1 hour at room temperature and then incubated overnight at 4°C with the primary antibodies rabbit anti-Iba-1 (Wako: 019- 19741, RRID:AB_839504) at 1:500 or rabbit anti-GFAP (Dako: Z0334, RRID: AB_10013382) at 1:1000 and then secondary antibodies (Alexa goat-647 anti-Rabbit) for 2 hours at room temperature. For BrdU/NeuN staining, one of every eight slices per mouse was chosen. Slices were washed in PBS with 0.1% Triton X three times for five minutes each before being incubated for in 2N HCl for 10 minutes at room temperature and then 20 minutes at 37°C. They were then placed in 0.1M Boric Acid buffer for 15 min and washed again three times with PBS. All slices were then incubated in starting block (ThermoFisher) with 0.3% Triton X for one hour before being staining in in PBS with 0.3% Triton X with rat anti-BrdU (Abcam: 6326 at 1:200), and mouse anti-NeuN (Millipore: MAB377 at 1:200) primary antibodies for 36-48 hours at 4°C and then secondary antibodies (Alexa Fluor 488 and 594 at 1:200) for 2 hours at room temperature. Slices were treated with 0.2% w/v Sudan Black in 70% EtOH for 5 min before mounting.

Confocal imaging and quantification

Slices were mounted with DAPI mounting media (Vectashield DAPI) and imaged with a confocal microscope (LSM 880, Zeiss). Reported cell densities were calculated based on distances in fixed tissue, uncorrected for volume changes due to fixation and mounting. All imaging and quantification were performed blind to the experimental group of the animal (PLX-treated or control).

Iba1 Quantification (Figure 2—Supplement 2)

For the 1- and 4-week timepoints, one z-stack per animal was imaged at 10X with pixel size 0.42 x 0.42 x 1 µm spanning the thickness of the slice. The number of frames used for maximum intensity projections was determined by the image with the smallest z-stack. For the 9-week timepoint, two z-stacks per animal were imaged at 20X and the counts from both were averaged. Stacks were imaged with pixel size 0.59 x 0.59 x 1 µm spanning 10 µm and converted to maximum intensity projections. For timepoints, the

bioRxiv preprint doi: https://doi.org/10.1101/714337; this version posted July 25, 2019. The copyright holder for this preprint (which was not certified by peer review) is the author/funder, who has granted bioRxiv a license to display the preprint in perpetuity. It is made available under aCC-BY-NC-ND 4.0 International license.

polygon tool was used to outline the granule cell layer in each image and the area was measured. Iba-1 positive cells were counted in this area manually using the Cell Counter plugin on maximum intensity projection images in ImageJ. Cells were counted only if the cell body was fully included in the image stack.

BrdU Quantification (Figure 2—Supplement 3)

For BrdU/NeuN, two z-stacks per OB (one centered dorsally and one centered ventrally) were taken at 20X with pixel size 0.52 x 0.52 x 0.89 µm spanning 9.8 µm. BrdU counts were performed using the automatic spots function in Imaris (Bitplane) with the same quality settings for spot detection for all images (quality threshold 2370, number of voxels threshold 524). Cells were counted as positive if they were located in the granule cell layer and were also positive for NeuN. The area of the granule cell layer in each image was measured in ImageJ, and the density of BrdU/NeuN positive cells was calculated for each image and averaged for all images for each mouse.

Spine quantification (Figure 5)

All images were 20-40 µm z-stacks with 0.42 z-step taken with a 63x oil immersion objective, and four fields of view were imaged per mouse. Care was taken to ensure minimal saturation (less than 5% of pixels). Dendrites that were judged to be sufficiently bright, well-separated from adjacent or overlapping dendrites, at least 40 µm long, and extending at an angle from the imaging plane less than 45 degrees were chosen for tracing in Imaris. Each dendrite and all its dendritic protrusions less than 10 µm in length were manually traced using the Filaments function. Data from each dendrite were exported in a text file and imported into Matlab for plotting. For spine density, the Imaris property “Filament No. Spine Terminal Pts” was used (meaning that branched spines were counted by the number of spine heads rather than attachment points). For spine head volume, the Imaris property “HeadVolume” was used. Imaris defines the spine head to be the terminal 25% of the spine’s length and calculates the volume in this compartment.

Electrophysiology (Figures 6 and 7)

Mice were deeply anesthetized with a mixture of ketamine (100 mg/kg) and xylazine (10 mg/kg) and perfused with ice-cold modified ACSF solution (in mM: 120 choline chloride, 25 glucose, 25 $NaHCO_3$, 2.5 KCl, 0.5 $CaCl_2$, 7 $MgSO_4$, 11.6 ascorbic acid, 3.1 pyruvic acid, 1.25 NaH_2PO_4). Brains were removed and placed in the same ice-cold modified ACSF. Horizontal slices (300 µm thick) of olfactory bulbs were cut using a vibratome (VT1000S; Leica, Germany). Slices were incubated in oxygenated holding solution (in mM: 119 NaCl, 26.2 $NaHCO_3$, 1 NaH_2PO_4*H_2O, 2.5 KCl, 22 glucose, 1.3 $CaCl_2$, 2.5 $MgSO_4$) at 33°C for at least 30 minutes before being transferred to oxygenated ACSF (in mM: 119 NaCl, 26.2 $NaHCO_3$, 1 NaH_2PO_4*H_2O, 2.5 KCl, 22 glucose, 2.5 $CaCl_2$, 1.3 $MgSO_4$). Extra slices were maintained in holding solution at room temperature. Whole-cell recordings (Bessel filtered at 1.8 kHz and acquired at 10 kHz) were performed using patch pipettes filled with internal solution (in mM: 125 potassium gluconate, 10 HEPES, 1 EGTA, 2.0 Na_2-ATP, 0.5 Na_3-GTP, 0.025 $CaCl_2$, 2 $MgCl_2$, pH 7.3) using a Multiclamp 700B amplifier (Molecular Devices, Palo Alto, CA) at 36 °C. Cells were visualized with dTomato and DIC with custom-built optics on a BX51WI microscope (Olympus Optical, Tokyo, Japan) and recorded with pClamp 10.3 (Molecular Devices). Cell identity was confirmed by the presence of fluorescence material in the patch pipet after membrane rupture and/or cell fill with Alexa Fluor 488, and only cells that had a proximal dendrite that extended from the soma in the direction of the EPL while remaining beneath the surface of the slice (i.e. cells that had dendrites that did not appear to have been cut during slicing) were targeted for patching. Patch pipets had 8-11 MΩ open tip resistance. Series resistance was not

bioRxiv preprint doi: https://doi.org/10.1101/714337; this version posted July 25, 2019. The copyright holder for this preprint (which was not certified by peer review) is the author/funder, who has granted bioRxiv a license to display the preprint in perpetuity. It is made available under aCC-BY-NC-ND 4.0 International license.

compensated. Cells were recorded in continuous 10-second sweeps for five minutes with a test pulse at the beginning of every sweep, which was used to calculate series resistance and holding current in Matlab for initial quality control. sEPSCs were recorded at -70 mV and sIPSCs were recorded at 0 mV. We waited at least one minute after breaking into the cell before beginning recording for sEPSCs and at least 30 seconds after switching the holding potential for sIPSCs; sEPSCs were always recorded first. Cells were recorded within 8 hours of slicing, and there did not appear to be any relationship between the time of recording and the frequency of synaptic events (data not shown). Experimenters were not blind to experimental group during recording.

Analysis

Experimenters were blind to experimental group during analysis. Cells with an initial series resistance of <50 MΩ were used for analysis. Sweeps that deviated from the average series resistance across the first three sweeps by more than 25% or had a holding current of more than 100 pA at -70 mV were excluded. The cell was excluded entirely if less than half of the recording sweeps remained after quality control. For each cell, separate test pulses (-10 mV, 20 ms) with 50 repetitions at 20 kHz were recorded before and after each set of recordings, and these files were used to calculate series resistance (based on the maximum current recorded at the beginning of the pulse), membrane resistance (based on the steady state current during the last 20% of the pulse), and cell capacitance (based on the time constant of an exponential fit between 20% and 80% of the current decay). Reported values in Figures 6 and 7 supplements are the means of these parameters from before and after the 5 minutes of sEPSC recordings. For sEPSCs and sIPSCs, all sweeps were concatenated for each cell (excluding 0.5 s around the test pulse), filtered with a 60Hz band-stop filter with five harmonics in Matlab, and exported into Mini Analysis v. 6.0.7 (Synaptosoft). sEPSCs were detected with the following parameters: threshold 5, period to search a local minimum 10000, time before a peak to baseline 15000, period to search a decay time 20000, fraction of peak to find a decay time 0.37, period to average a baseline 1000, area threshold 20, number of points to average for peak 1, direction of peak “negative.” After the initial detection step, “Scan and detect double peaks” was selected. sIPSCs were detected with the following parameters: threshold 8, period to search a local minimum 10000, time before a peak to baseline 6000, period to search a decay time 20000, fraction of peak to find a decay time 0.37, period to average a baseline 1000, area threshold 80, number of points to average for peak 1, direction of peak “positive.” In both cases, the detection was manually inspected, and the timepoints spanning any sections of the trace that exhibited increased noise (typically due to fluctuations in seal quality that caused many obviously false positive events) were noted. Event data was exported to a text file and imported into Matlab and noisy sections were excluded before further analysis. Cells that had many noisy sections were excluded. This included 3 control cells and 2 PLX cells for EPSCs and 2 control cells and 4 PLX cells for IPSCs (Figure 6) as well as 3 control and 3 PLX cells for EPSCs and 8 control cells and 9 PLX cells for IPSCs (Figure 7).

bioRxiv preprint doi: https://doi.org/10.1101/714337; this version posted July 25, 2019. The copyright holder for this preprint (which was not certified by peer review) is the author/funder, who has granted bioRxiv a license to display the preprint in perpetuity. It is made available under aCC-BY-NC-ND 4.0 International license.

Table 1

1	ethyl tiglate
2	ethyl valerate
3	Valeric acid
4	allyl butyrate
5	(-) carvone
6	2-methoxypyrazine
7	isoeugenol
8	allyl tiglate
9	valeraldehyde
10	isoamyl acetate
11	anisole
12	ethyl propionate
13	propyl acetate
14	2-heptanone
15	acetophenone

bioRxiv preprint doi: https://doi.org/10.1101/714337; this version posted July 25, 2019. The copyright holder for this preprint (which was not certified by peer review) is the author/funder, who has granted bioRxiv a license to display the preprint in perpetuity. It is made available under aCC-BY-NC-ND 4.0 International license.

Methods references

Allen, M., Poggiali, D., Whitaker, K., Marshall, T. R., & Kievit, R. (2018). Raincloud plots: a multi-platform tool for robust data visualization. *PeerJ Preprints*, *6*, e27137v1. https://doi.org/10.1044/1092-4388(2010/09-0205)

Arganda-Carreras, I., Kaynig, V., Rueden, C., Eliceiri, K. W., Schindelin, J., Cardona, A., & Seung, H. S. (2017). Trainable Weka Segmentation: A machine learning tool for microscopy pixel classification. *Bioinformatics*, *33*(15), 2424–2426. https://doi.org/10.1093/bioinformatics/btx180

Dombeck, D., & Tank, D. (2014). Two-photon imaging of neural activity in awake mobile mice. *Cold Spring Harbor Protocols*, *2014*(7), 726–736. https://doi.org/10.1101/pdb.top081810

Dubbs, A., Guevara, J., & Yuste, R. (2016). moco: Fast Motion Correction for Calcium Imaging. *Frontiers in Neuroinformatics*, *10*(February), 1–7. https://doi.org/10.3389/fninf.2016.00006

Grimaud, J., & Murthy, V. N. (2018). How to monitor breathing in laboratory rodents: a review of the current methods. *Journal of Neurophysiology*, *120*(2), 624–632. https://doi.org/10.1152/jn.00708.2017

Guo, Z. V., Hires, S. A., Li, N., O'Connor, D. H., Komiyama, T., Ophir, E., … Svoboda, K. (2014). Procedures for behavioral experiments in head-fixed mice. *PLoS ONE*, *9*(2). https://doi.org/10.1371/journal.pone.0088678

Hioki, H., Kuramoto, E., Konno, M., Kameda, H., Takahashi, Y., Nakano, T., … Kaneko, T. (2009). High-level transgene expression in neurons by lentivirus with Tet-Off system. *Neuroscience Research*, *63*(2), 149–154. https://doi.org/10.1016/j.neures.2008.10.010

Jung, S., Aliberti, J., Graemmel, P., Sunshine, M. J., Kreutzberg, G. W., Sher, A., & Littman, D. A. N. R. (2000). Analysis of Fractalkine Receptor CX 3 CR1 Function by Targeted Deletion and Green Fluorescent Protein Reporter Gene Insertion, *20*(11), 4106–4114.

Wallace, J. L., Wienisch, M., & Murthy, V. N. (2017). Development and Refinement of Functional Properties of Adult-Born Neurons. *Neuron*, *96*, 883–896. https://doi.org/10.1016/j.neuron.2017.09.039

Wienisch, M., & Murthy, V. N. (2016). Population imaging at subcellular resolution supports specific and local inhibition by granule cells in the olfactory bulb. *Scientific Reports*, *6*(April), 29308. https://doi.org/10.1038/srep29308

Willmore, B., & Tolhurst, D. J. (2001). Characterizing the sparseness of neural codes. *Network*, *12*(3), 255–270. https://doi.org/10.1088/0954-898X/12/3/302

bioRxiv preprint doi: https://doi.org/10.1101/714337; this version posted July 25, 2019. The copyright holder for this preprint (which was not certified by peer review) is the author/funder, who has granted bioRxiv a license to display the preprint in perpetuity. It is made available under aCC-BY-NC-ND 4.0 International license.

Figure 1

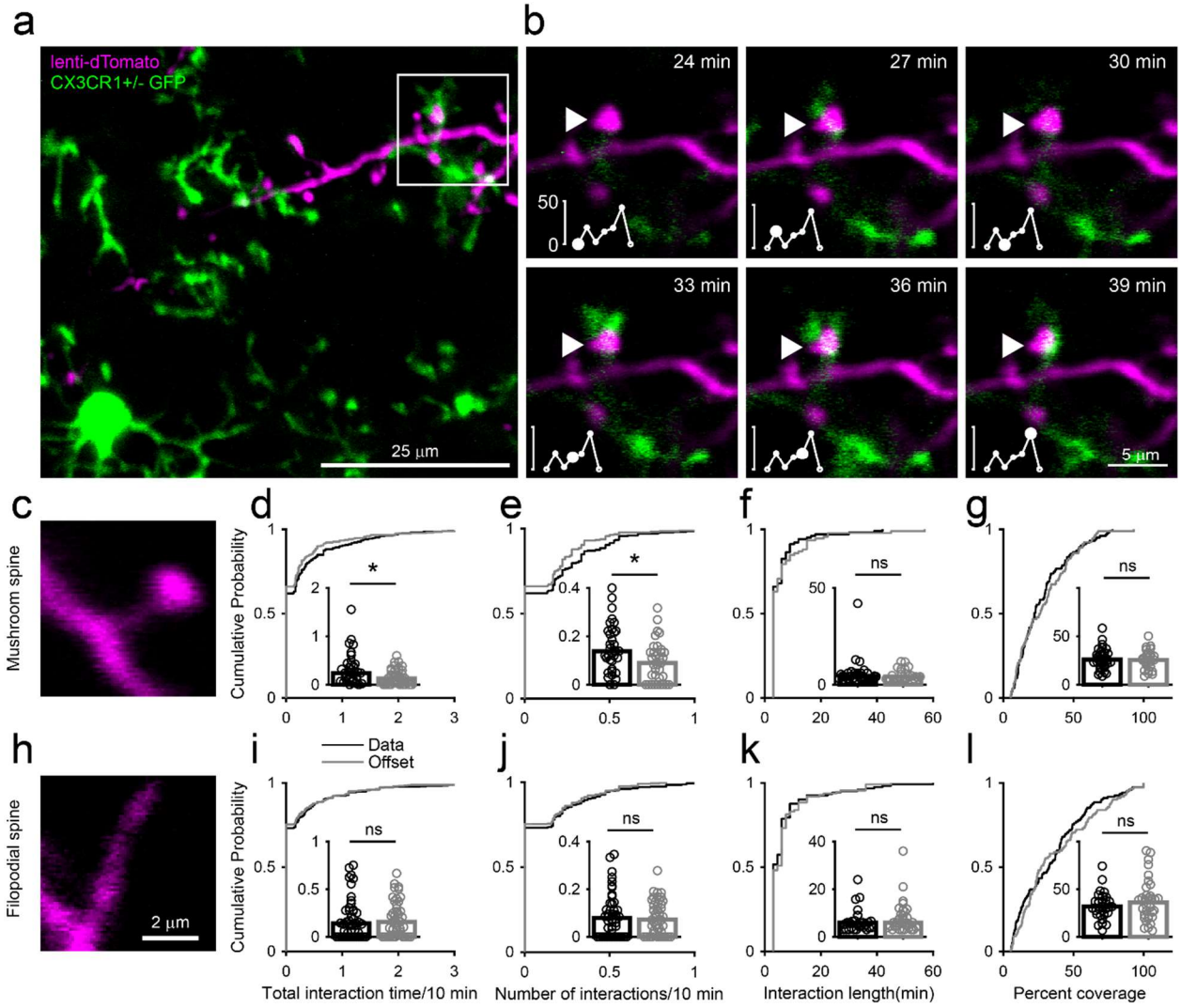

bioRxiv preprint doi: https://doi.org/10.1101/714337; this version posted July 25, 2019. The copyright holder for this preprint (which was not certified by peer review) is the author/funder, who has granted bioRxiv a license to display the preprint in perpetuity. It is made available under aCC-BY-NC-ND 4.0 International license.

Figure 1: Microglia preferentially interact with mushroom spines on developing abGCs

a) Maximum intensity projection (10 µm volume at the first imaging timepoint) showing dTomato-labeled abGCs in a CX3CR1-GFP heterozygous mouse imaged 4 weeks after lentivirus injection. Brightness and contrast adjusted for display only.
b) Single plane time series showing the region marked in (A). Inset shows the calculated percent microglial coverage for the spine marked with the arrowhead (images shown for 6 frames, 7th frame not shown but the value is plotted, showing the end of the interaction) with the larger circle marking the value for the corresponding frame. Brightness and contrast adjusted with the same parameters for each timepoint for display only.
c) Single plane image showing an example of a spine classified as a mushroom spine because the spine head is wider and brighter than the spine neck.
d) Cumulative distribution showing total interaction time (normalized to 10 minutes) for all mushroom spines in the real data ("Data") compared to values calculated from translating the microglial channel relative to the dendritic imaging channel ("Offset"). Inset, the median total interaction time across all dendrites, each marked with a circle (value for each dendrite is the median time across all mushroom spines) was significantly higher in the real data (Wilcoxon rank sum test, $z = 2.34$, $p = 0.020$).
e) Cumulative distribution showing the number of interactions (normalized to 10 minutes) for all mushroom spines. Inset, the median number of interactions across all dendrites (value for each dendrite is the median number across all mushroom spines) was significantly higher in the real data (Wilcoxon rank sum test, $z = 2.45$, $p = 0.014$).
f) Cumulative distribution showing interaction length (for spines that had at least one frame that met the criteria for an interaction, see Methods). Inset, the median interaction length across all dendrites (value for each dendrite is the median interaction length across all interactions for all mushroom spines) was not different between real and offset data (Wilcoxon rank sum test, $z = 0.25$, $p = 0.80$).
g) Cumulative distribution showing maximum percent coverage (median across all interactions for a given spine for spines that had at least one frame that met the criteria for an interaction). Inset, the median maximum percent coverage across all dendrites (value for each dendrite is the median interaction length across all interactions for all mushroom spines) was not different between real and offset data (Wilcoxon rank sum test, $z = 0.092$, $p = 0.93$).
h) Single plane image of a spine classified as a filopodial spine because it has no clear spine head.
i) Cumulative distribution showing total interaction time (normalized to 10 minutes) for all filopodial spines in the real data ("Data") compared to values calculated from translating the microglial channel relative to the dendritic imaging channel ("Offset"). Inset, the median total interaction time across all dendrites, each marked with a circle (value for each dendrite is the median time across all filopodial spines) was not different between real and shuffled data (Wilcoxon rank sum test, $z = -0.29$, $p = 0.77$).
j) Cumulative distribution showing the number of interactions (normalized to 10 minutes) for all filopodial spines. Inset, the median number of interactions across all dendrites (value for each dendrite is the median number across all filopodial spines) was not different between real and offset data (Wilcoxon rank sum test, $z = 0.0084$, $p = 0.99$).
k) Cumulative distribution showing interaction length (for spines that had at least one frame that met the criteria for an interaction, see Methods). Inset, the median interaction length across all

bioRxiv preprint doi: https://doi.org/10.1101/714337; this version posted July 25, 2019. The copyright holder for this preprint (which was not certified by peer review) is the author/funder, who has granted bioRxiv a license to display the preprint in perpetuity. It is made available under aCC-BY-NC-ND 4.0 International license.

dendrites (value for each dendrite is the median interaction length across all interactions for all filopodial spines) was not different between real and offset data (Wilcoxon rank sum test, z = -0.50, p = 0.62).

l) Cumulative distribution showing maximum percent coverage (median across all interactions for a given spine for spines that had at least one frame that met the criteria for an interaction). Inset, the median maximum percent coverage across all dendrites (value for each dendrite is the median interaction length across all interactions for all filopodial spines) was not different between real and offset data (Wilcoxon rank sum test, z = -0.72, p = 0.47).

Bars represent medians across individual dendrites (circles).

n = 726 spines (271 mushroom spines and 455 filopodial spines) from 48 dendrites combined at 1, 2, 3, and 4 weeks post injection in 3 mice

*p<0.05

bioRxiv preprint doi: https://doi.org/10.1101/714337; this version posted July 25, 2019. The copyright holder for this preprint (which was not certified by peer review) is the author/funder, who has granted bioRxiv a license to display the preprint in perpetuity. It is made available under aCC-BY-NC-ND 4.0 International license.

Figure 2

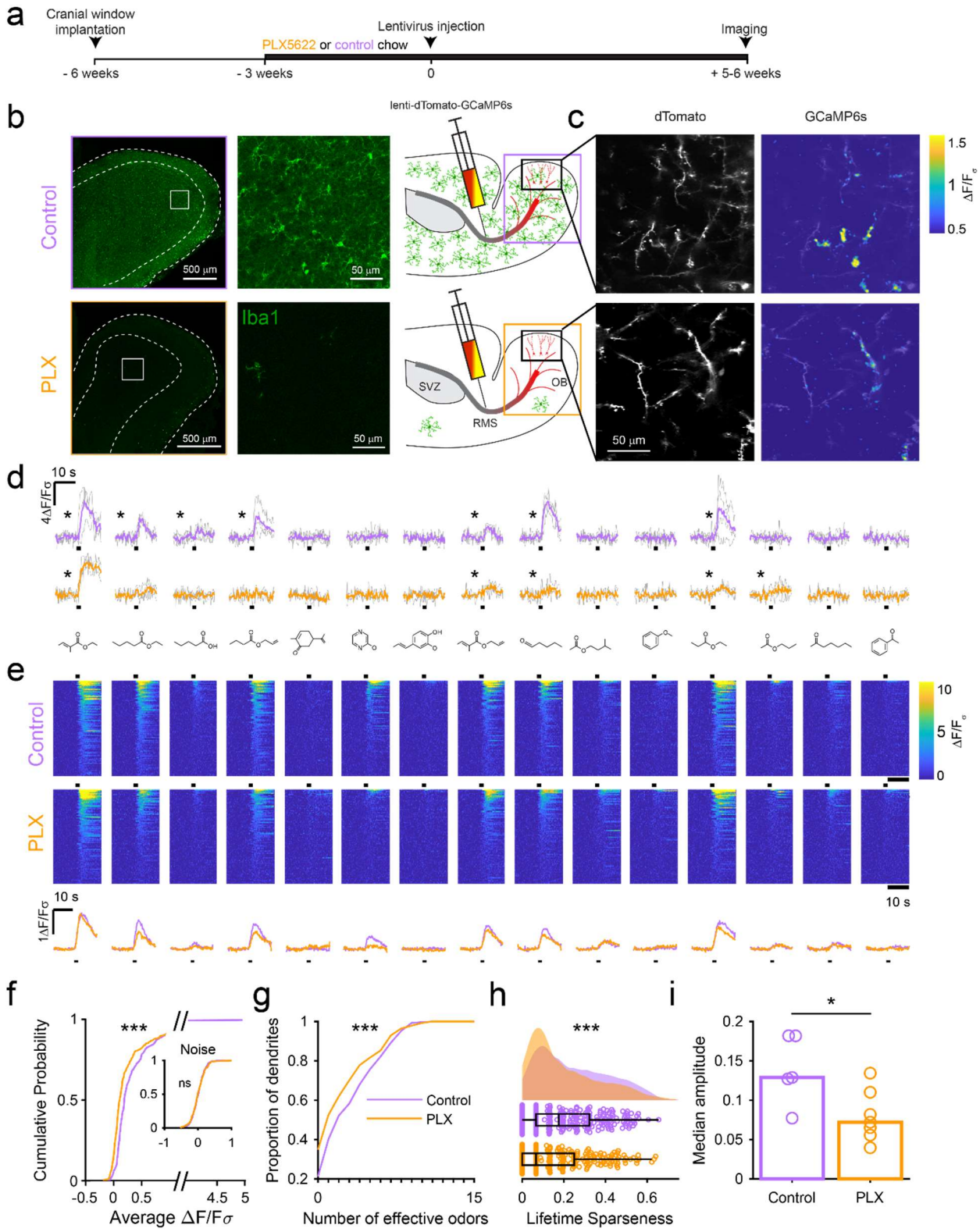

bioRxiv preprint doi: https://doi.org/10.1101/714337; this version posted July 25, 2019. The copyright holder for this preprint (which was not certified by peer review) is the author/funder, who has granted bioRxiv a license to display the preprint in perpetuity. It is made available under aCC-BY-NC-ND 4.0 International license.

Figure 2: Microglia ablation during development reduces odor-evoked responses of abGCs in anesthetized mice.

a) Experimental timeline for microglia ablation during development of abGCs. A cranial window was implanted and 3 weeks later mice were given control or PLX5622-containing chow for the remainder of the experiment. After 3 weeks of chow consumption, a lentivirus was injected into the RMS to label abGCs, which were imaged 5-6 weeks later.
b) Left, images of Iba1 staining in the olfactory bulb of control (top) and PLX-treated (bottom) mice. White squares show the locations of the enlarged insets. Dotted lines mark the upper edge of the glomerular and granule cell layers. Right, schematic showing injection of a lentivirus encoding dTomato and GCaMP6s and microglia ablation.
c) Example fields of view showing an average intensity projection of dTomato structural images of abGC dendrites (left) and overlaid heatmaps of GCaMP6s-recorded activity (right) in response to ethyl valerate in control (top) and PLX5622-treated (bottom) mice.
d) GCaMP6s traces showing odor responses of example ROIs from control (top) and PLX-treated (bottom) mice (chosen to have the same ranked response to the first odor). Gray traces represent responses on individual trials and colored trace is the mean across trials. Individual trial traces were median filtered over three frames before averaging for presentation. *, odor responses for which the mean response was above threshold
e) Heatmap traces from the 100 ROIs with the largest odor-evoked Ca2+ signals across all mice ranked separately for each of 16 odors (molecular structures shown above). Black bar denotes odor time. Bottom, mean response time course for each odor across all ROIs.
f) Cumulative distribution showing that the distribution of responses (averaged across odors for each dendrite) is shifted to the left in PLX-treated mice (Two sample Kolmogorov–Smirnov test for probability distributions, $D = 0.25$, $p = 2.56e-08$) while the noise distributions constructed from blank trials are not different ($D = 0.042$, $p = 0.96$).
g) Cumulative distribution showing the number of effective odors (odors that evoked responses above the ROC threshold 0.39, which was calculated across all dendrites from both groups). The median number of effective odors was significantly lower in the PLX-treated group (Wilcoxon rank sum test, $z = 3.49$, $p = 4.86e-04$).
h) Raincloud plot showing the distribution of lifetime sparseness across all dendrites. Above, kernel density estimate. Below, boxplot showing the median, interquartile range (box), and 1.5 times the interquartile range (whiskers) superimposed on a dot plot of all the data (one dot per dendrite). Median lifetime sparseness was significantly lower in the PLX-treated group (Wilcoxon rank sum test, $z = 5.53$, $p = 4.18e-04$).
i) Plot showing the median response amplitude across all dendrites from each mouse; bars represent the group median and dots represent each mouse. Response amplitude was lower in PLX-treated mice (Wilcoxon rank sum test, rank sum = 45, $p = 0.048$).

n = 287 dendrites from 5 control mice and 277 dendrites from 7 PLX-treated mice

*$p<0.05$, **$p<0.01$, ***$p<0.001$

bioRxiv preprint doi: https://doi.org/10.1101/714337; this version posted July 25, 2019. The copyright holder for this preprint (which was not certified by peer review) is the author/funder, who has granted bioRxiv a license to display the preprint in perpetuity. It is made available under aCC-BY-NC-ND 4.0 International license.

Figure 2.1

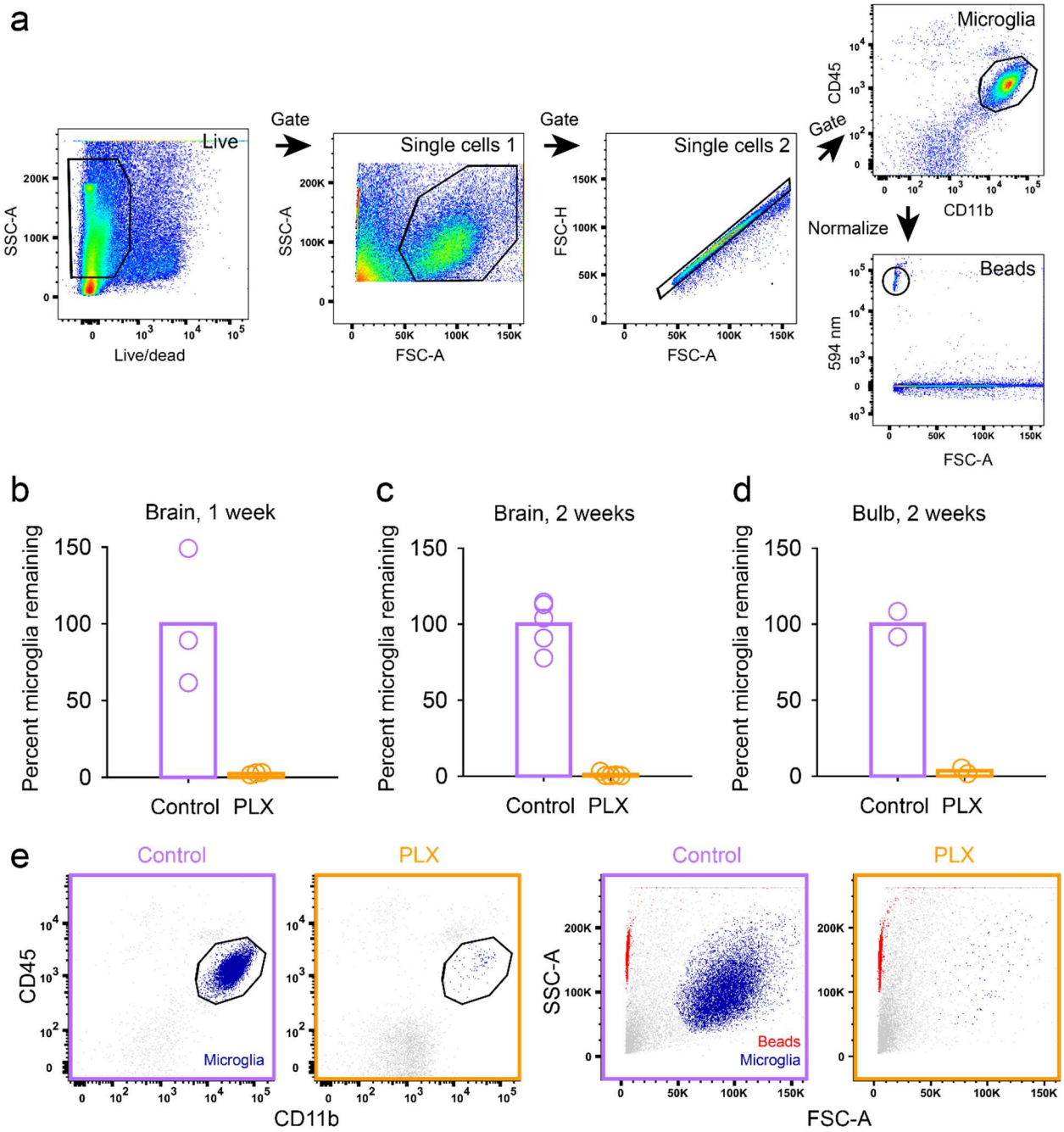

Figure 2 Supplement 1

a) Microglia cells were gated on CD45^{intermediate} and CD11b^{high} using the following gating strategy: Debris and dead cells were excluded based on the fluorescent intensity of a dead cell stain. Next, single cells where determined based on of their light scattering properties (first by side over forward scatter, SSC-A/FSC-A, and second by forward scatter height over area, FSC-H/FSC-A). The counting beads were identified based on their fluorescent emission at 594 nm.

b) Plot showing the percent of live microglia remaining (normalized to the mean of the controls) in mice treated with PLX compared to controls (number of microglia in each sample normalized to

bioRxiv preprint doi: https://doi.org/10.1101/714337; this version posted July 25, 2019. The copyright holder for this preprint (which was not certified by peer review) is the author/funder, who has granted bioRxiv a license to display the preprint in perpetuity. It is made available under aCC-BY-NC-ND 4.0 International license.

counting beads) in whole brain samples after 1 week of control or PLX diet demonstrating 97.4% ablation.

c) Plot showing the percent of live microglia remaining in mice treated with PLX (normalized to the mean of the controls) compared to controls (number of microglia in each sample normalized to counting beads) in whole brain samples after 1 week of control or PLX diet, demonstrating 99.0% ablation.

d) Plot showing the percent of live microglia remaining in mice treated with PLX (normalized to the mean of the controls) compared to controls measured via FACs olfactory bulb samples after 2 weeks of control or PLX diet, demonstrating 96.4% ablation.

e) Interrogation of light scattering properties (SSC-A/FSC-A) independent of surface marker labeling revealed that hardly any cells remained in the microglia enriched samples after treatment with PLX compared to control samples. This becomes visually more apparent when microglia cells ($CD45^{intermediate}$, $CD11b^{high}$, control and PLX-treated plots on left) are backpropagated to SSC-A/FSC-A plots on right (in dark blue). Note that counting beads can be observed in red.

Bars represent the mean across mice (circles).

Whole brain: n = 5 control and 5 PLX mice

OB: n = 2 control and 2 PLX samples (each sample contained both OBs from 2 littermates which were combined after dissection)

bioRxiv preprint doi: https://doi.org/10.1101/714337; this version posted July 25, 2019. The copyright holder for this preprint (which was not certified by peer review) is the author/funder, who has granted bioRxiv a license to display the preprint in perpetuity. It is made available under aCC-BY-NC-ND 4.0 International license.

Figure 2.2

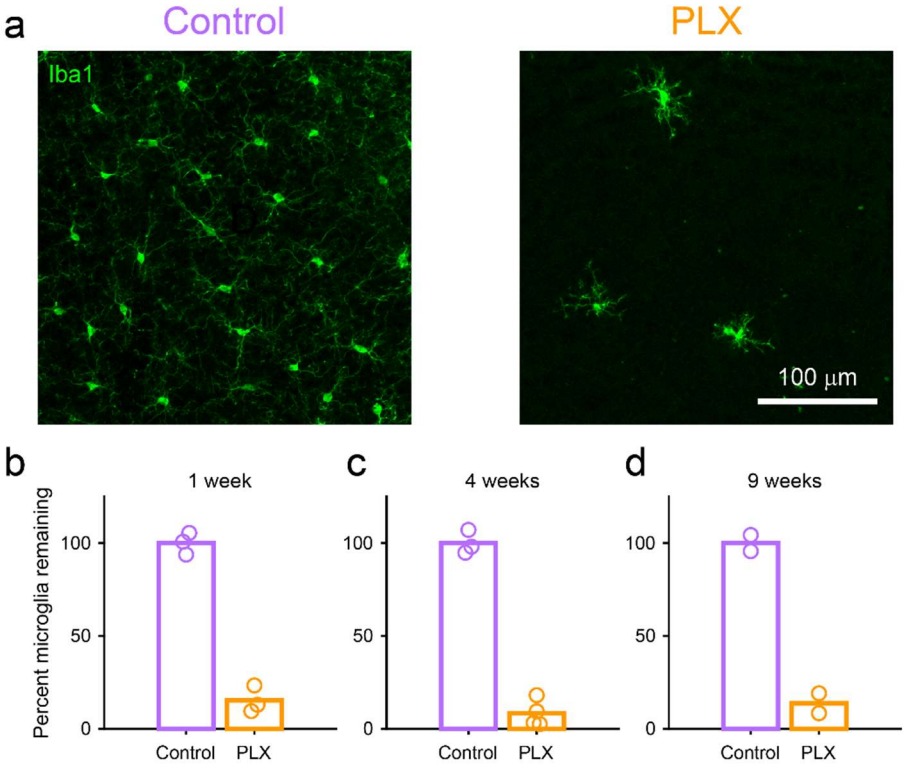

Figure 2 Supplement 2

a) Maximum intensity projection showing microglia stained with Iba1 in the granule cell layer of the olfactory bulb in control (left) and PLX-treated (right) mice after 4 weeks of treatment.
b) Plot showing the percent of microglia remaining in mice treated with PLX compared to control littermates based on counting of cell bodies stained with Iba1 after 1 week of treatment, demonstrating 84.7% ablation.
c) Percent microglia remaining after 4 weeks of treatment (same mice used for spine quantification in Figure 5), demonstrating 91.7% ablation.
d) Percent microglia remaining after 9 weeks of treatment (PLX mice are the same mice used for imaging at the 9 weeks timepoint in Figure 4 Supplement 1 and control mice are age-matched controls), demonstrating 86.2% ablation.

Bars represent the mean across mice (circles).

n = 3 mice (1 week), 4 mice (4 weeks), and 2 mice (9 weeks)

bioRxiv preprint doi: https://doi.org/10.1101/714337; this version posted July 25, 2019. The copyright holder for this preprint (which was not certified by peer review) is the author/funder, who has granted bioRxiv a license to display the preprint in perpetuity. It is made available under aCC-BY-NC-ND 4.0 International license.

Figure 2.3

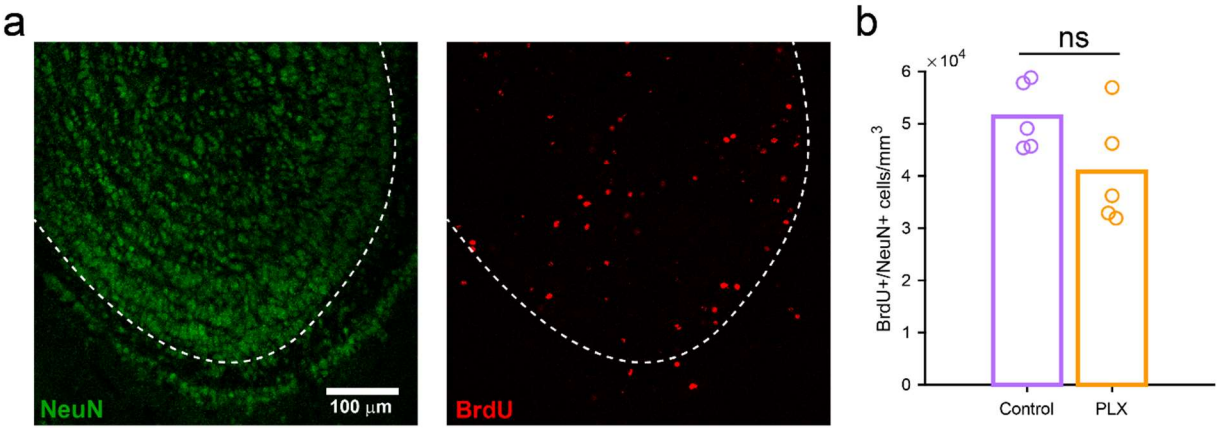

Figure 2 Supplement 3

a) Maximum intensity projection showing NeuN staining (left) and BrdU staining (right) in the olfactory bulb. Dotted line indicates boundary of the granule cell layer, where positive cells were quantified.
b) Plot showing the density of BrdU+/NeuN+ cells per mm^3 in the granule cell layer of the olfactory bulb in control mice and mice treated with PLX for 4 weeks, beginning 3 days after BrdU injection. The density was not different between groups (Two sample t-test, $t = 1.89$, $p = 0.30$).

Bars represent the mean across mice (circles).

n = 5 control and 5 PLX-treated mice

bioRxiv preprint doi: https://doi.org/10.1101/714337; this version posted July 25, 2019. The copyright holder for this preprint (which was not certified by peer review) is the author/funder, who has granted bioRxiv a license to display the preprint in perpetuity. It is made available under aCC-BY-NC-ND 4.0 International license.

Figure 2.4

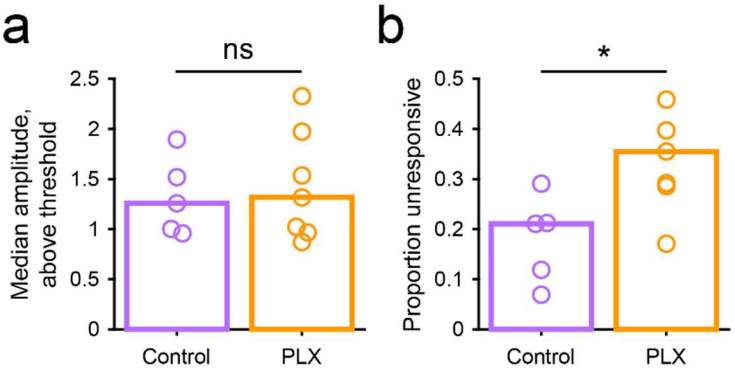

a) The median response amplitude for all responses above threshold from each mouse was not different between PLX-treated and control mice (Wilcoxon rank sum test, rank sum = 30, p = 0.76).
b) The proportion of dendrites not responding to any of the odors in the panel was higher in PLX-treated mice (Wilcoxon rank sum test, rank sum = 19, p = 0.030).

Bars represent the median across individual mice (circles).

n = 5 control mice and 7 PLX-treated mice

*p<0.05

bioRxiv preprint doi: https://doi.org/10.1101/714337; this version posted July 25, 2019. The copyright holder for this preprint (which was not certified by peer review) is the author/funder, who has granted bioRxiv a license to display the preprint in perpetuity. It is made available under aCC-BY-NC-ND 4.0 International license.

Figure 3

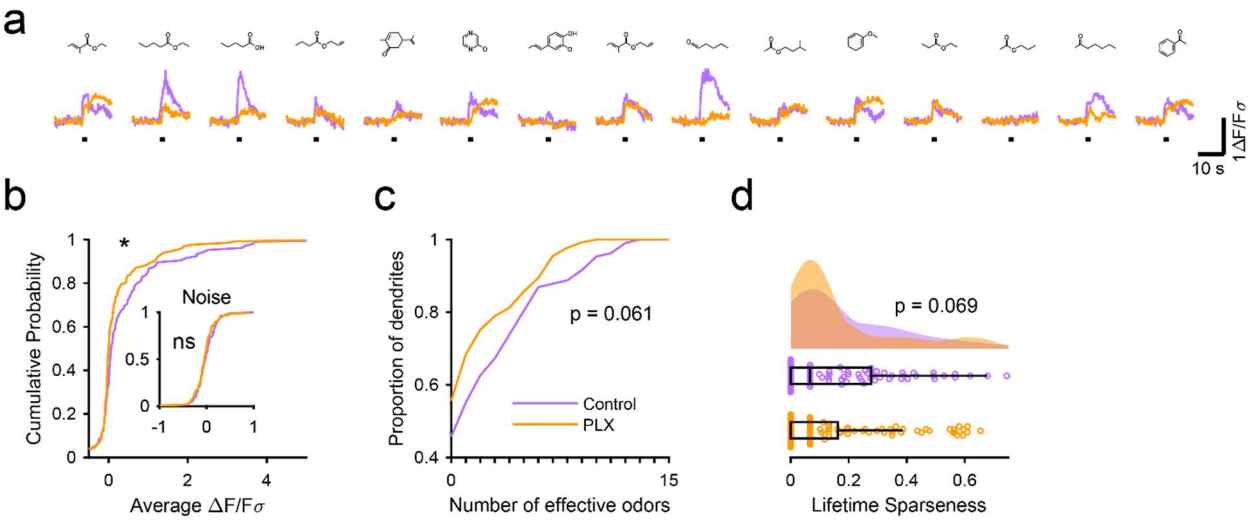

Figure 3: Microglia ablation during development reduces odor-evoked responses of abGCs in awake mice.

a) Mean response time course for each odor across all ROIs. Black bar denotes odor time.
b) Cumulative distribution showing that the distribution of responses (averaged across odors for each dendrite) is shifted to the left in PLX-treated mice (Two sample Kolmogorov–Smirnov test for probability distributions, D = 0.18, p = 0.037) while the noise distributions constructed from blank trials are not different (D = 0.11, p = 0.45).
c) Cumulative distribution showing the number of effective odors (odors that evoked responses above the ROC threshold 0.52, which was calculated across all dendrites from both groups). There was a trend toward a lower median number of effective odors in the PLX-treated group (Wilcoxon rank sum test, z = 1.88, p = 0.061).
d) Raincloud plot showing the distribution of lifetime sparseness across all dendrite. Above, kernel density estimate. Below, boxplot showing the median, interquartile range (box), and 1.5 times the interquartile range (whiskers) superimposed on a dot plot of all the data (one dot per dendrite). There was a trend toward lower median lifetime sparseness in the PLX-treated group (Wilcoxon rank sum test, z = 1.82, p = 0.069).

n = 105 dendrites from 3 control mice and 132 dendrites from 4 PLX-treated mice

*p<0.05

bioRxiv preprint doi: https://doi.org/10.1101/714337; this version posted July 25, 2019. The copyright holder for this preprint (which was not certified by peer review) is the author/funder, who has granted bioRxiv a license to display the preprint in perpetuity. It is made available under aCC-BY-NC-ND 4.0 International license.

Figure 3.1

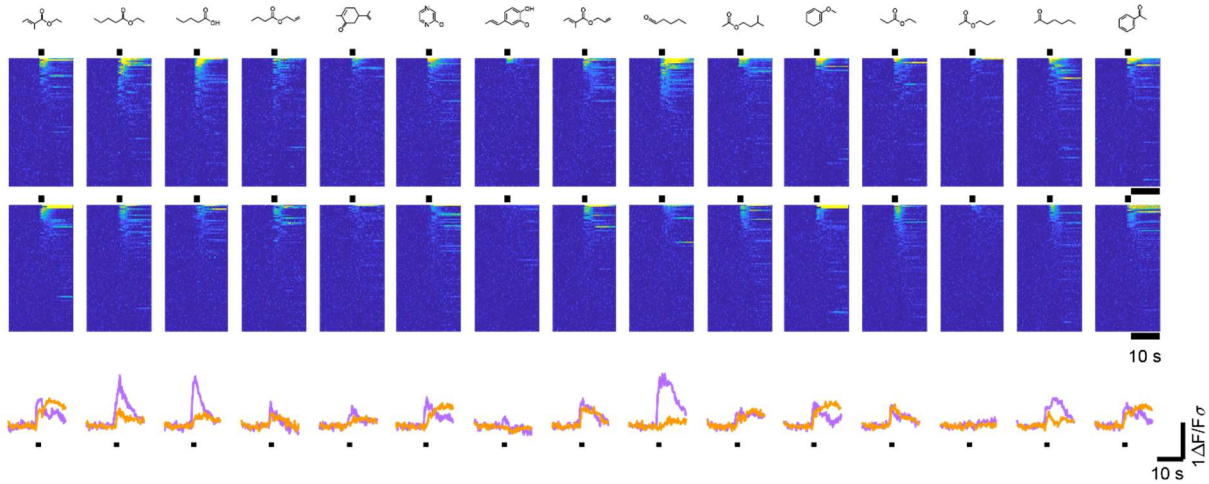

Figure 3 Supplement 1

Heatmap traces from the 100 ROIs with the largest odor-evoked Ca2+ signals across all mice ranked for each of 16 odors (molecular structures shown above). Black bar denotes odor time. Mean traces shown below are the same as those from Figure 3.

bioRxiv preprint doi: https://doi.org/10.1101/714337; this version posted July 25, 2019. The copyright holder for this preprint (which was not certified by peer review) is the author/funder, who has granted bioRxiv a license to display the preprint in perpetuity. It is made available under aCC-BY-NC-ND 4.0 International license.

Figure 3.2

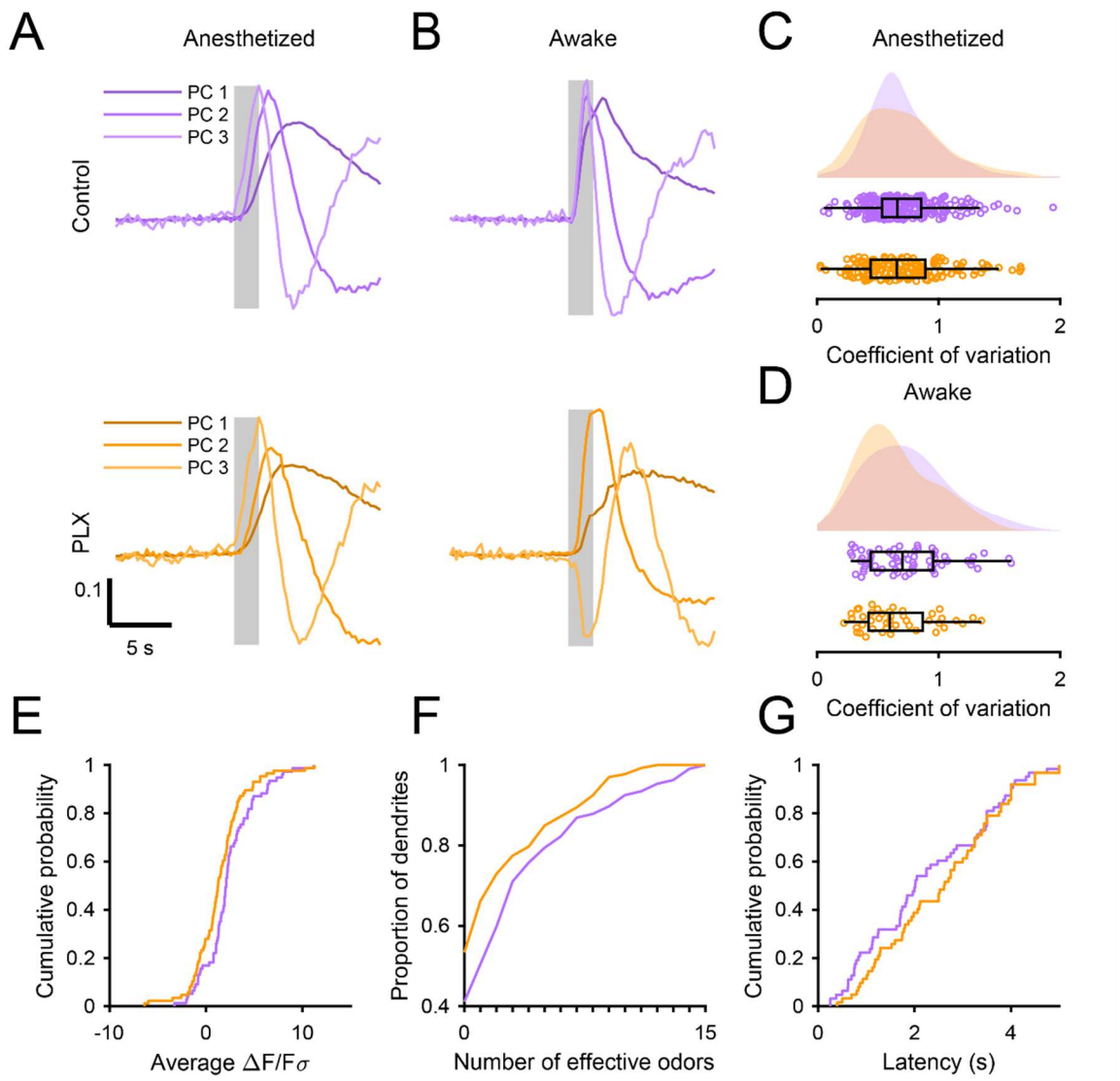

Figure 3 Supplement 2

a) Top, the first three principal components (PCs) obtained from PCA of the temporal profiles of responses of all abGC dendrites ($\Delta F/F_\sigma$ traces, GCaMP6s) in anesthetized control mice to all odors. Percent variance explained: 36.3%, 4.19%, 1.85% for the first three PCs, respectively. Bottom, The first three PCs for odor responses in anesthetized PLX-treated mice. Percent variance explained: 33.7%, 3.82%, 1.96%. Shading indicates the odor presentation period (2 s). The timecourses of responses for the odor analysis period (5 s after odor onset) for the first three PCs was not different between control and PLX-treated mice ($p = 0.41$).

b) Top, the first three PCs for odor responses in awake control mice. Percent variance explained: 43.7%, 12.6%, 3.36%. Bottom, the first three PCs for odor responses in awake PLX-treated mice. Percent variance explained: 44.9%, 10.2%, 2.86%. The timecourses of responses for the odor

bioRxiv preprint doi: https://doi.org/10.1101/714337; this version posted July 25, 2019. The copyright holder for this preprint (which was not certified by peer review) is the author/funder, who has granted bioRxiv a license to display the preprint in perpetuity. It is made available under aCC-BY-NC-ND 4.0 International license.

analysis period for the first three PCs were significantly different between control and PLX-treated mice (p = 0.011).

c) Raincloud plot showing the distribution of coefficient of variation values for all dendrites in anesthetized mice averaged across all odors for which the dendrite had a mean response above threshold (ROC thresholds calculated separately for control (threshold = 0.37) and PLX (threshold = 0.5) to ensure the same proportion of true responses). Above, kernel density estimate. Below, boxplot showing the median, interquartile range (box), and 1.5 times the interquartile range (whiskers) superimposed on a dot plot of all the data (one dot per cell, unless the cell had no responses above threshold in which case it is not included). The median CVs were not significantly different (Control: 0.59, PLX: 0.62, Wilcoxon rank sum test, z = 0.58, p = 0.56).

d) Raincloud plot showing the distribution of coefficient of variation values for all dendrites in awake mice averaged across all odors for which the dendrite had a response above threshold (ROC thresholds calculated separately for control (threshold = 0.46) and PLX (threshold = 0.85) to ensure the same proportion of true responses). The median CVs were not significantly different (Control: 0.55, PLX: 0.48, Wilcoxon rank sum test, z = 1.47, p = 0.14).

e) Cumulative distribution (responses averaged across odors for each dendrite) showing that the distribution of responses detected with event analysis (ROC threshold calculated across both groups combined, event detected during the odor analysis period if 6 or more frames were at least 2.6 standard deviations above baseline) is not significantly different in PLX-treated mice (Two sample Kolmogorov–Smirnov test for probability distributions, D = 0.18, p = 0.23).

f) Cumulative distribution showing the number of effective odors (odors for which an event was detected in at least one repetition). The median number of effective odors was lower in the PLX-treated group (Wilcoxon rank sum test, z = 2.09, p = 0.037).

g) Cumulative distribution showing that the latency from odor onset to event detection (averaged across odors for each dendrite) is not significantly different in PLX-treated mice (Two sample Kolmogorov–Smirnov test for probability distributions, D = 0.17, p = 0.31).

*p<0.05

bioRxiv preprint doi: https://doi.org/10.1101/714337; this version posted July 25, 2019. The copyright holder for this preprint (which was not certified by peer review) is the author/funder, who has granted bioRxiv a license to display the preprint in perpetuity. It is made available under aCC-BY-NC-ND 4.0 International license.

Figure 3.3

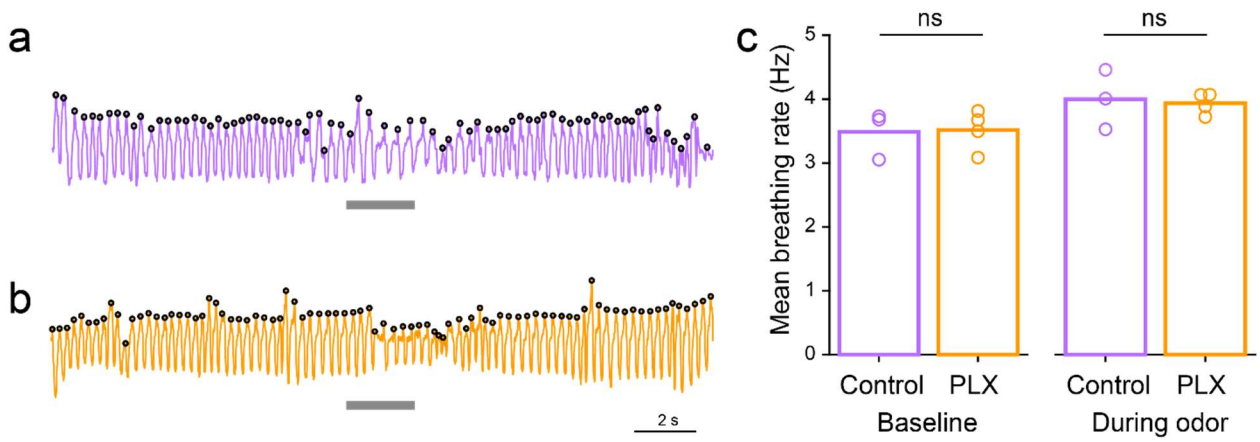

Figure 3 Supplement 3

a) Example trace showing breathing recordings during one trial from a control mouse. The gray bar indicates the time the odor is on and the black circles indicate sniffs that were detected.
b) Example trace showing breathing recordings during one trial from a PLX-treated mouse.
c) Mean breathing rate during baseline periods (10 s before the odor comes on) and during the odor period (2 s) calculated from all sniffs recorded in all trials from each mouse. The breathing rates in the two groups were not different during the baseline period (Two sample t test, $t = -0.11$, $p = 0.91$) or the odor period (Two sample t test, $t = 0.25$, $p = 0.81$).

Bars represent the mean across mice (circles).

n = 3 control mice (Baseline: 15,086 detected sniffs, Odor: 2,895 detected sniffs) and 4 PLX-treated mice (Baseline: 19,248 detected sniffs, Odor: 3,468 detected sniffs)

bioRxiv preprint doi: https://doi.org/10.1101/714337; this version posted July 25, 2019. The copyright holder for this preprint (which was not certified by peer review) is the author/funder, who has granted bioRxiv a license to display the preprint in perpetuity. It is made available under aCC-BY-NC-ND 4.0 International license.

Figure 4

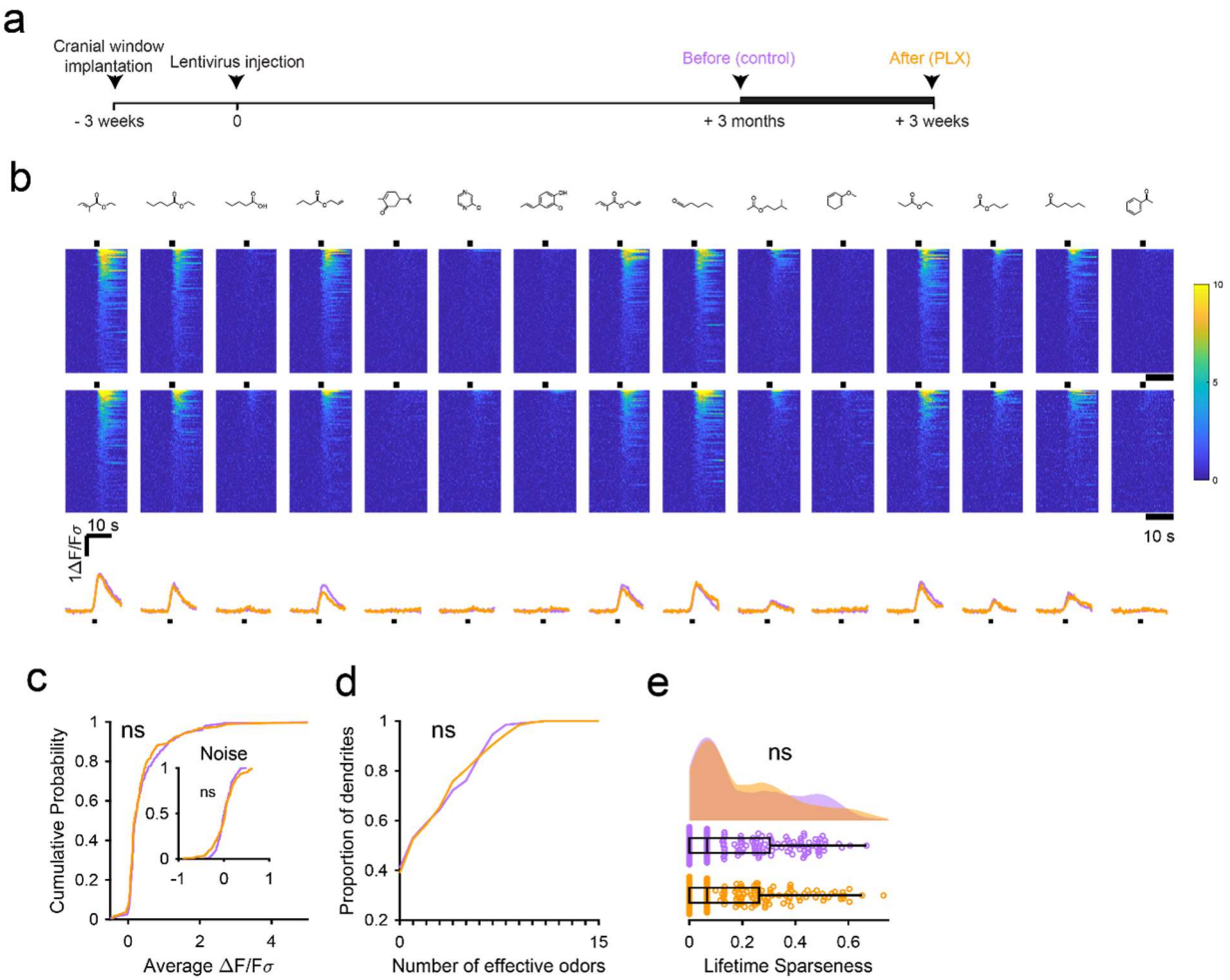

Figure 4: Microglia ablation after development has no effect on odor-evoked responses of abGCs

a) Experimental timeline for microglia ablation after development of abGCs. AbGCs were labeled via lentivirus injection and allowed to mature for 3 months. A control imaging session was performed immediately before administration of PLX chow and the second imaging session occurred 3 weeks later.
b) Heatmap traces from the 100 ROIs with the largest odor-evoked Ca2+ signals across all mice ranked for each of 16 odors (molecular structures shown above). Black bar denotes odor time. Bottom, mean response time course for each odor across all ROIs.
c) Cumulative distribution showing that the distribution of responses (averaged across odors for each dendrite) is not different before and after PLX diet administration (Two sample Kolmogorov–Smirnov test, D = 0.087, p = 0.89) and the noise distributions constructed from blank trials are also not different (D = 0.11, p = 0.15).
d) Cumulative distribution showing the number of effective odors (odors that evoked responses above the ROC threshold 0.53, which was calculated across all dendrites from both groups). The median number of effective odors was not different between groups (Wilcoxon rank sum test, z = -0.14, p = 0.89).

bioRxiv preprint doi: https://doi.org/10.1101/714337; this version posted July 25, 2019. The copyright holder for this preprint (which was not certified by peer review) is the author/funder, who has granted bioRxiv a license to display the preprint in perpetuity. It is made available under aCC-BY-NC-ND 4.0 International license.

e) Raincloud plot showing the distribution of lifetime sparseness across all dendrite. Above, kernel density estimate. Below, boxplot showing the median, interquartile range (box), and 1.5 times the interquartile range (whiskers) superimposed on a dot plot of all the data (one dot per dendrite). Median lifetime sparseness was not different between groups (Wilcoxon rank sum test, z = 0.0073, p = 0.99).

n = 198 dendrites before and 185 dendrites after 3 weeks of PLX administration from 3 mice

bioRxiv preprint doi: https://doi.org/10.1101/714337; this version posted July 25, 2019. The copyright holder for this preprint (which was not certified by peer review) is the author/funder, who has granted bioRxiv a license to display the preprint in perpetuity. It is made available under aCC-BY-NC-ND 4.0 International license.

Figure 4.1

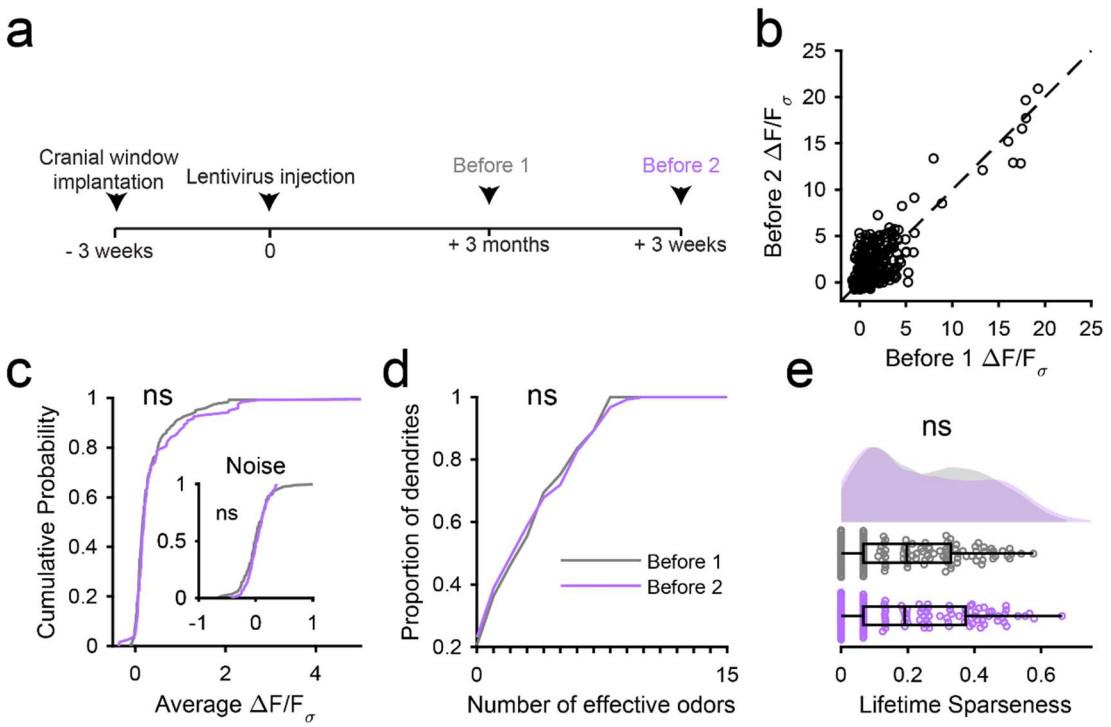

Figure 4 Supplement 1

a) Experimental timeline for microglia ablation after development of abGCs. AbGCs were labeled via lentivirus injection and allowed to mature for 3 months. One imaging session was performed and a second was performed 3 weeks later in which the same dendrites were imaged again (the second is the same "Control" imaging session from the main figure).
b) Scatterplot showing the responses of all dendrite-odor pairs plotted for the first imaging session compared to the second imaging session. Dotted line is unity. Linear correlation coefficient R2 = 0.73, p = 0.
c) Cumulative distribution showing that the distribution of responses (averaged across odors for each dendrite) is not different between the two imaging sessions (Two sample Kolmogorov–Smirnov test for probability distributions, D = 0.097, p = 0.61) and the noise distributions constructed from blank trials are also not different (D = 0.11, p = 0.48).
d) Cumulative distribution showing the number of effective odors (odors that evoked responses above the ROC threshold 0.39, which was calculated across all dendrites from both groups). The median number of effective odors was not different between groups (Wilcoxon rank sum test, z = 0.20, p = 0.84).
e) Raincloud plot showing the distribution of lifetime sparseness for all dendrites. Above, kernel density estimate. Below, boxplot showing the median, interquartile range (box), and 1.5 times the interquartile range (whiskers) superimposed on a dot plot of all the data (one dot per dendrite). The median lifetime sparseness values were not significantly different (Wilcoxon rank sum test, z = 0.30, p = 0.76).

n = 121 dendrites from 3 mice (same mice from the main figure)

bioRxiv preprint doi: https://doi.org/10.1101/714337; this version posted July 25, 2019. The copyright holder for this preprint (which was not certified by peer review) is the author/funder, who has granted bioRxiv a license to display the preprint in perpetuity. It is made available under aCC-BY-NC-ND 4.0 International license.

Figure 4.2

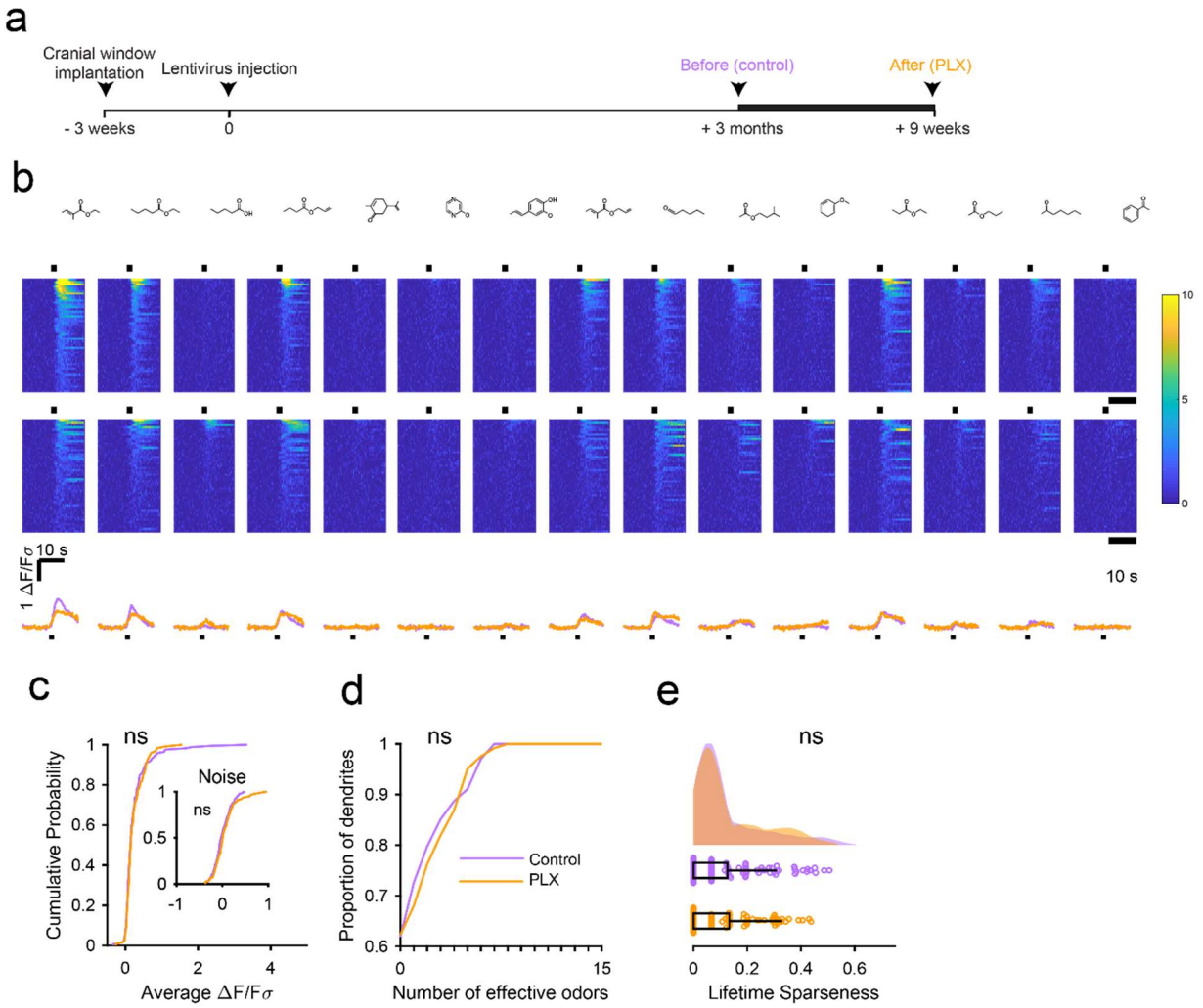

Figure 4 Supplement 2

a) Experimental timeline for microglia ablation after development of abGCs. AbGCs were labeled via lentivirus injection and allowed to mature for 3 months. A control imaging session was performed immediately before administration of PLX chow and the second imaging session occurred 9 weeks later.
b) Heatmap traces from the 100 ROIs with the largest odor-evoked Ca2+ signals across all mice ranked for each of 16 odors (molecular structures shown above). Black bar denotes odor time. Bottom, mean response time course for each odor across all ROIs.
c) Cumulative distribution showing that the distribution of responses (averaged across odors for each dendrite) is not different before and after PLX diet administration (Two sample Kolmogorov–Smirnov test for probability distributions, D = 0.089, p = 0.61) and the noise distributions constructed from blank trials are also not different (D = 0.14, p = 0.095).
d) Cumulative distribution showing the number of effective odors (odors that evoked responses above the ROC threshold 0.78, which was calculated across all dendrites from both groups). The

bioRxiv preprint doi: https://doi.org/10.1101/714337; this version posted July 25, 2019. The copyright holder for this preprint (which was not certified by peer review) is the author/funder, who has granted bioRxiv a license to display the preprint in perpetuity. It is made available under aCC-BY-NC-ND 4.0 International license.

median number of effective odors was not different between groups (Wilcoxon rank sum test, z = -0.17, p = 0.87).

e) Raincloud plot showing the distribution of lifetime sparseness for all dendrites in control and PLX-treated mice. Above, kernel density estimate. Below, boxplot showing the median, interquartile range (box), and 1.5 times the interquartile range (whiskers) superimposed on a dot plot of all the data (one dot per dendrite). Median lifetime sparseness was not different between groups (Wilcoxon rank sum test z = -0.26, p = 0.79).

n = 168 dendrites before and 122 dendrites after 9 weeks of PLX administration from 3 mice (1 mouse was also included in the 3 weeks group that is shown in the main figure)

bioRxiv preprint doi: https://doi.org/10.1101/714337; this version posted July 25, 2019. The copyright holder for this preprint (which was not certified by peer review) is the author/funder, who has granted bioRxiv a license to display the preprint in perpetuity. It is made available under aCC-BY-NC-ND 4.0 International license.

Figure 5

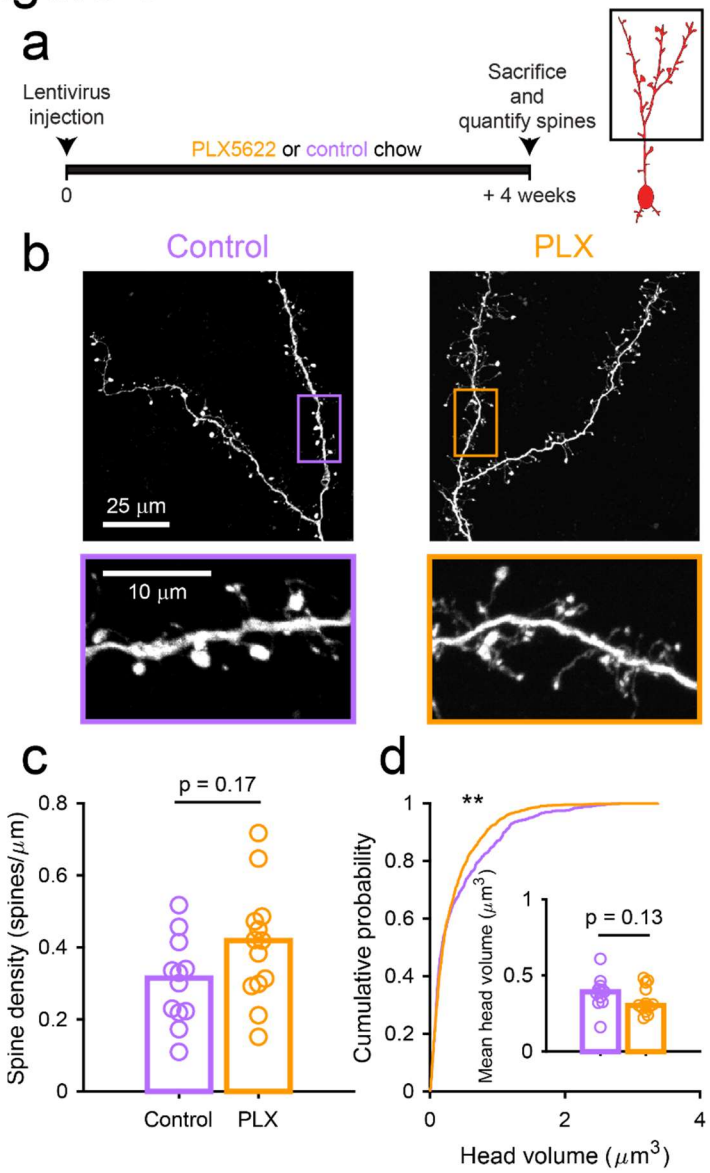

Figure 5: Microglia ablation during development reduces spine head volume in abGCs

a) Experimental timeline for microglia ablation during development of abGCs. Mice were given control or PLX5622-containing chow on the same day that a lentivirus was injected into the RMS to label abGCs. Spine numbers and morphology were quantified 4 weeks later.
b) Above, sample images showing two apical dendrites from one cell that were analyzed in a control mouse (left) and PLX-treated mouse (right). Below, insets from the images shown above, showing spine morphology in more detail.
c) Spine density averaged across 1-5 apical dendrites from each abGC. There was no difference in spine density between the two groups (Wilcoxon rank sum test, $z = -1.39$, $p = 0.17$).
d) Cumulative distribution showing the volume of all spines analyzed. The distribution is shifted toward smaller spines in PLX-treated mice (Two sample Kolmogorov–Smirnov test, $D = 0.080$, $p = 0.0044$). Inset, head volume averaged across all spines in each cell. The distributions were not

bioRxiv preprint doi: https://doi.org/10.1101/714337; this version posted July 25, 2019. The copyright holder for this preprint (which was not certified by peer review) is the author/funder, who has granted bioRxiv a license to display the preprint in perpetuity. It is made available under aCC-BY-NC-ND 4.0 International license.

significantly different when the volume of all spines was averaged per cell (Wilcoxon rank sum test, z = 1.50, p = 0.13).

Bars indicate medians across cells (circles).

n = 740 spines from 12 abGCs from 3 control mice and 1316 spines from 13 abGCs from 4 PLX mice

**p<0.01

bioRxiv preprint doi: https://doi.org/10.1101/714337; this version posted July 25, 2019. The copyright holder for this preprint (which was not certified by peer review) is the author/funder, who has granted bioRxiv a license to display the preprint in perpetuity. It is made available under aCC-BY-NC-ND 4.0 International license.

Figure 6

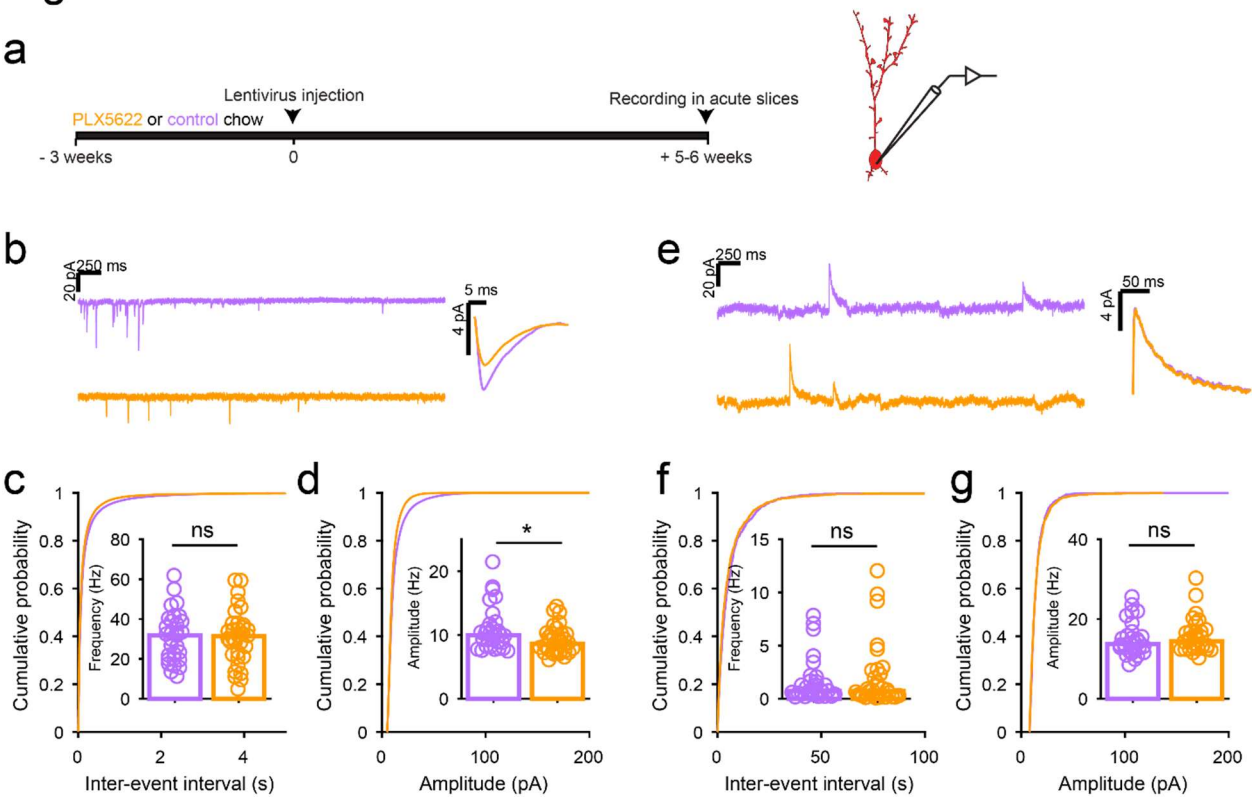

Figure 6: Microglia ablation during abGC development reduces the amplitude of excitatory synaptic currents but does not affect inhibitory synaptic currents

a) Experimental timeline for electrophysiological recording in abGCs
b) Left, sample sections from raw traces recorded from abGCs in control (top) and PLX-treated (bottom) mice. Right, median EPSCs across all EPSCs detected from all mice.
c) Cumulative distribution showing the inter-event intervals from all recorded events. Inset, median frequency for all events from each cell. The distributions were not significantly different when all events were averaged for each cell (Wilcoxon rank sum test, z = 0.090, p = 0.93).
d) Cumulative distribution showing the amplitudes from all recorded events. Inset, median amplitude for all events from each cell. Cells from PLX-treated mice had lower event amplitudes (Wilcoxon rank sum test, z = 2.35, p = 0.019).
e) Left, Sample sections from raw traces recorded from abGCs in control (top) and PLX-treated (bottom) mice. Right, median IPSCs across all IPSCs detected from all mice.
f) Cumulative distribution showing the inter-event intervals from all recorded events. Inset, median frequency for all events from each cell. The distributions were not significantly different when all events were averaged for each cell (Wilcoxon rank sum test, z = 0.31, p = 0.76).
g) Cumulative distribution showing the amplitudes from all recorded events. Inset, median amplitude for all events from each cell. The distributions were not significantly different when all events were averaged for each cell (Wilcoxon rank sum test, z = -0.85, p = 0.39).

Bars indicate medians across cells (circles).

For EPSCs: n = 30 abGCs from 4 control mice and 33 abGCs from 4 PLX mice

bioRxiv preprint doi: https://doi.org/10.1101/714337; this version posted July 25, 2019. The copyright holder for this preprint (which was not certified by peer review) is the author/funder, who has granted bioRxiv a license to display the preprint in perpetuity. It is made available under aCC-BY-NC-ND 4.0 International license.

For IPSCs: n = 29 abGCs from 4 control mice and 30 abGCs from 4 PLX mice (same mice in both cases and cells used for both EPSCs and IPSCs if the recordings met criteria stated in Methods)
*p<0.05

bioRxiv preprint doi: https://doi.org/10.1101/714337; this version posted July 25, 2019. The copyright holder for this preprint (which was not certified by peer review) is the author/funder, who has granted bioRxiv a license to display the preprint in perpetuity. It is made available under aCC-BY-NC-ND 4.0 International license.

Figure 6.1

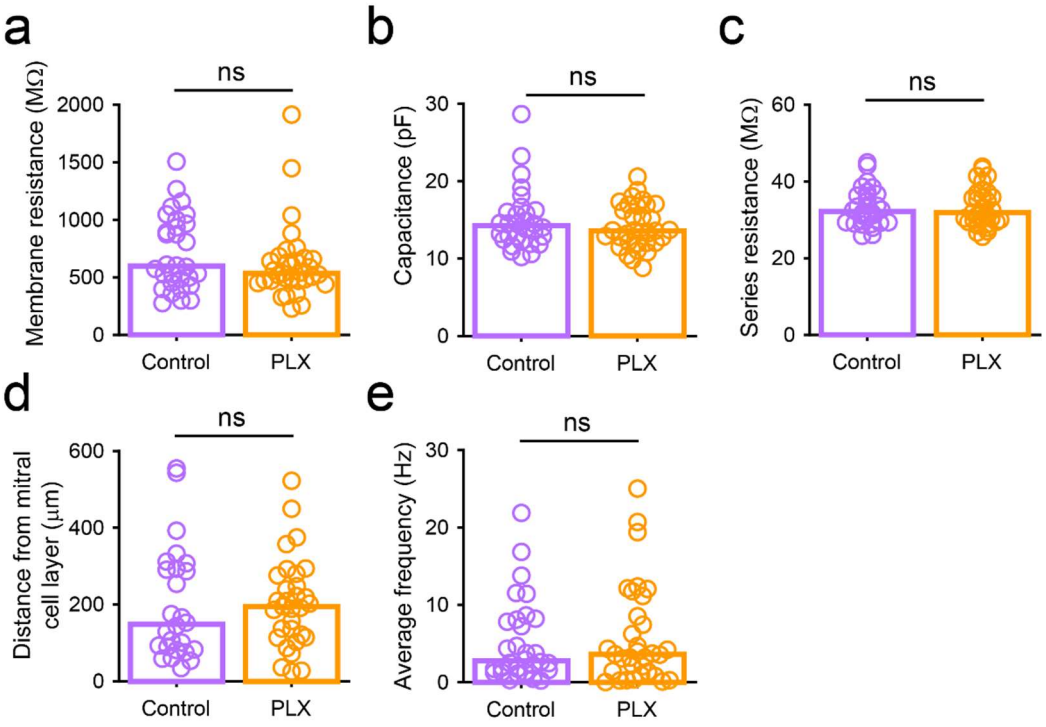

Figure 6 Supplement 1

a) Membrane resistance (mean of measurements taken before and after EPSC recordings) in abGCs. There was no difference between the two groups (Wilcoxon rank sum test, z = 1.01, p = 0.31).
b) Membrane capacitance (mean of measurements taken before and after EPSC recordings) in abGCs. There was no difference between the two groups (Wilcoxon rank sum test, z = 0.52, p = 0.61).
c) Series resistance (mean of measurements taken before and after EPSC recordings) during abGC recordings. There was no difference between the two groups (Wilcoxon rank sum test, z = 0.048, p = 0.96).
d) Distance of the cell body from the mitral cell layer (measured in 2D, not taking into account depth from the surface of the slice) for all cells recorded. Both superficial and deep abGCs were included in the dataset and there was no difference in the mean distance to the mitral cell layer between the two groups (Wilcoxon rank sum test, z = -0.52, p = 0.60).
e) Average frequency of EPSCs across the entire recording period in abGCs. There was no difference between groups (Wilcoxon rank sum test, z = -0.10, p = 0.92).

Bars indicate medians across cells (circles).

n = 30 abGCs from 4 control mice and 33 abGCs from 4 PLX mice

bioRxiv preprint doi: https://doi.org/10.1101/714337; this version posted July 25, 2019. The copyright holder for this preprint (which was not certified by peer review) is the author/funder, who has granted bioRxiv a license to display the preprint in perpetuity. It is made available under aCC-BY-NC-ND 4.0 International license.

Figure 7

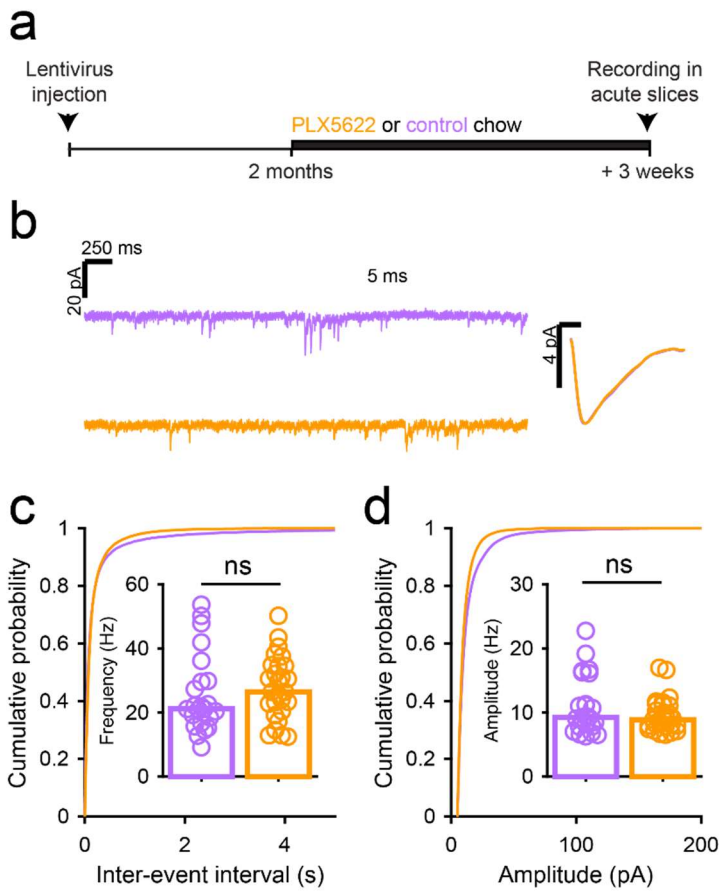

Figure 7: Microglia ablation after abGC development has no effect on excitatory synaptic currents

a) Experimental timeline for electrophysiological recordings in abGCs after their development
b) Left, Sample sections from raw traces recorded from abGCs in control (top) and PLX-treated (bottom) mice. Right, median EPSCs detected from all mice.
c) Cumulative distribution showing the inter-event intervals from all recorded events. Inset, median frequency for all events from each cell. The distributions were not significantly different when all events were averaged for each cell (Wilcoxon rank sum test, z = -1.27, p = 0.21).
d) Cumulative distribution showing the amplitudes from all recorded events. Inset, median amplitude for all events from each cell. The distributions were not significantly different when all events were averaged for each cell (Wilcoxon rank sum test, z = 0.41, p = 0.68).

Bars indicate medians across cells (circles).
n = 23 abGCs from 3 control mice and 27 abGCs from 3 PLX mice
*p<0.05

bioRxiv preprint doi: https://doi.org/10.1101/714337; this version posted July 25, 2019. The copyright holder for this preprint (which was not certified by peer review) is the author/funder, who has granted bioRxiv a license to display the preprint in perpetuity. It is made available under aCC-BY-NC-ND 4.0 International license.

Figure 7.1

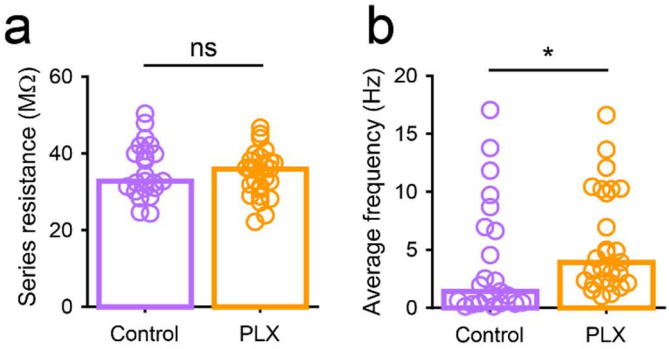

Figure 7 Supplement 1

a) Series resistance (mean of measurements taken before and after EPSC recordings) during abGC recordings. There was no difference between the two groups (Wilcoxon rank sum test, z = 0.27, p = 0.79).
b) Average frequency of EPSCs across the entire recording period in abGCs. There was a higher average EPSC frequency in PLX-treated mice (Wilcoxon rank sum test, z = -2.32, p = 0.02).

Bars indicate medians across cells (circles).

n = 30 abGCs from 4 control mice and 33 abGCs from 4 PLX mice

*p<0.05

bioRxiv preprint doi: https://doi.org/10.1101/714337; this version posted July 25, 2019. The copyright holder for this preprint (which was not certified by peer review) is the author/funder, who has granted bioRxiv a license to display the preprint in perpetuity. It is made available under aCC-BY-NC-ND 4.0 International license.

Figure 7.2

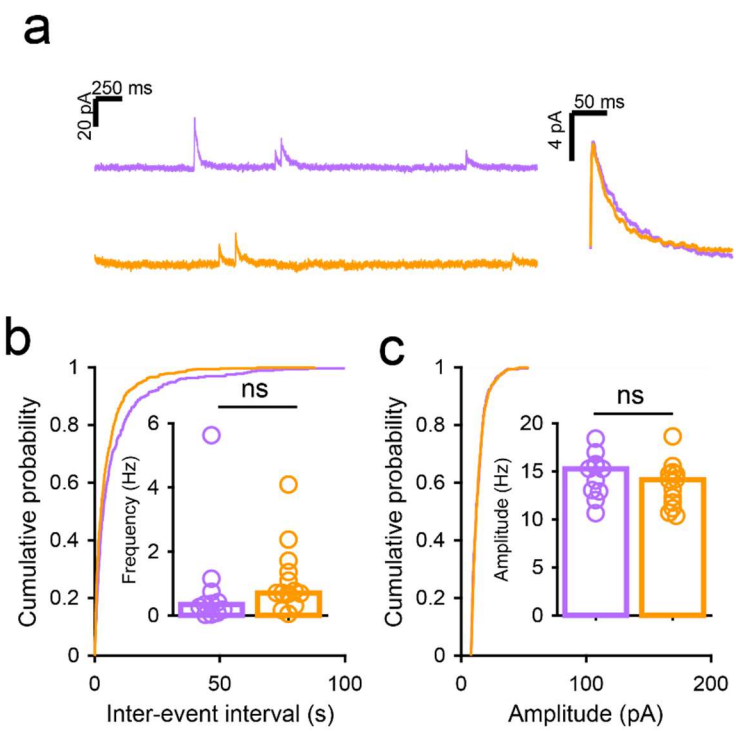

Figure 7 Supplement 2

a) Left, Sample sections from raw traces recorded from abGCs in control (top) and PLX-treated (bottom) mice. Right, median IPSCs calculated across all IPSCs detected from all mice.
b) Cumulative distribution showing the inter-event intervals from all recorded events. Inset, median frequency for all events from each cell. The distributions were not significantly different when all events were averaged for each cell (Wilcoxon rank sum test, z = -1.62, p = 0.10).
c) Cumulative distribution showing the amplitudes from all recorded events. Inset, median amplitude for all events from each cell. The distributions were not significantly different when all events were averaged for each cell (Wilcoxon rank sum test, t = 1.10, p = 0.27).

Bars indicate medians across cells (circles).

n = 11 abGCs from 3 control mice and 13 abGCs from 3 PLX mice

bioRxiv preprint doi: https://doi.org/10.1101/714337; this version posted July 25, 2019. The copyright holder for this preprint (which was not certified by peer review) is the author/funder, who has granted bioRxiv a license to display the preprint in perpetuity. It is made available under aCC-BY-NC-ND 4.0 International license.

Video 1. Z stack showing microglia and abGC dendrites. Movie showing the entire field of view at the beginning of the imaging session for the example shown in Figure 1. The z stack volume spans 29 µm and was taken at 32 dpi. The analysis in Figure 1 was performed on individual planes from such z stacks.

Video 2. Time series showing interactions between microglia and dendritic spines of abGCs. Movie showing a single plane taken from the z stack in Video 1 across 48 minutes of imaging (images taken 3 minutes apart). The time course of the interaction between a microglial process and the mushroom spine shown in the example in Figure 1 can be observed. The analysis in Figure 1 was performed on individual planes from such time series.